ESA Climate Change Initiative (CCI+)
Essential Climate Variable (ECV)

Antarctica_Ice_Sheet_cci+ (AIS_cci+)

Algorithm Theoretical Basis Document (ATBD)

Prime & Science Lead: Andrew Shepherd

Northumbria University, Newcastle upon Tyne, United Kingdom

Technical Officer: Anna Maria Trofaier

ESA ECSAT, Didcot, United Kingdom

Consortium: DTU Microwaves and Remote Sensing Group (DTU-N)

DTU Geodynamics Group (DTU-S)

Environmental Earth Observation IT GmbH (ENVEO)

Deutsches Zentrum für Luft- und Raumfahrt (DLR) Remote Sensing Technology Institute (IMF)

Northumbria University (NU)

Science [&] Technology AS (ST)

Technische Universität Dresden (TUDr)

University College London (UCL/MSSL)

Signatures page

Prepared by	Jan Wuite Project Scientist, ENVEO	JWuite
Checked by	Andrew Shepherd Science Leader, NU	
Issued by	Daniele Fantin, Project Manager, S&T	Daniele Fantin Digitally signed by Daniele Fantin Date: 2025.02.07 14:31:21 CET
Approved by	Anna Maria Trofaier ESA Technical Officer	Digitally signed by Anna Maria Trofaier Date: 2025.02.21 13:32:40 Z

Table of Contents

Change Log

Issue	Author	Affected Section	Change	Status
1.0	J. Wuite, ENVEO	All	Document Creation	
2.0	J. Wuite, ENVEO	All	Updated for Phase 2	Released to ESA

Acronyms and Abbreviations

Acronym	Explanation
AIS	Antarctic Ice Sheet
ADP	Algorithm Development Plan
AIS_cci+	Antarctic Ice Sheets CCI project Extension
API	Antarctic Peninsula
ATBD	Algorithm Theoretical Basis Document
CCI(+)	Climate Change Initiative (Extension)
CFL	Calving Front Location
CONAE	Comisión Nacional de Actividades Espaciales
DEM	Digital Elevation Model
DLR	Deutsches Zentrum für Luft- und Raumfahrt
DTU	Danish Technical University
EAIS	East Antarctic Ice Sheet
ECV	Essential Climate Variable
ENVEO	ENVironmental Earth Observation GmbH
EO	Earth Observation
ESA	European Space Agency
GLL	Grounding Line Location
GLM	Grounding Line Migration
GMB	Gravimetric Mass Balance
ISCL	Ice Shelf Coast Line
IV	Ice Velocity
IV-TCM	Ice Velocity Tidal Correction Module
IVC	Ice Velocity Change
MFID	Mass Flux Ice Discharge
MPC	Mission Performance Cluster
SEC	Surface Elevation Change
SL	Science Lead
SOW	Statement of Work
ST	Science & Technology AS
TOPS	Terrain Observation by Progressive Scans
TUD	Technical University of Dresden
UB	University of Bristol
UCL	University College London
UN	University of Northumbria
WAIS	West Antarctic Ice Sheet
NASA	National Aeronautics and Space Administration
SAR	Synthetic Aperture Radar
InSAR	Interferometric SAR
ML	Machine Learning

1 Introduction

1.1 Purpose and Scope

This document contains the Algorithm Theoretical Basis Document (ATBD) for Phase 2 of the Antarctic Ice Sheet CCI+ (AIS CCI+) in accordance with the contract and SoW [AD1 and AD2]. The ATBD describes the scientific background and principle of the algorithms, their expected or known accuracy and performance, input and output data, as well as capabilities and limitations, for the essential climate variable (ECV) products from Earth Observation (EO) satellite data for the Antarctic Ice Sheet (AIS) which include [RD1]:

1. Surface Elevation Change (SEC)
2. Ice Velocity (IV)
3. Ice Velocity Change (IVC)
4. Gravimetric Mass Balance (GMB)
5. Grounding Line Location (GLL)
6. Grounding Line Migration (GLM)
7. Ice Shelf CoastLines (ISCL)

This document contains the Algorithm Theoretical Basis for the Antarctic Ice Sheet cci (AIS_cci) project for CCI+ Phase 1, in accordance to contract and SoW [AD1 and AD2]. The ATBD describes the scientific background and principle of the algorithms, their expected or known accuracy and performance, input and output data, as well as capabilities and limitations.

1.2 Document Structure

This document is structured as follows:

- Chapter 1 provides an introduction to the document.
- Chapters 2 to 7 provide descriptions of planned algorithm developments for each ECV parameter.

1.3 Applicable and Reference Documents

Table 1.1: List of Applicable Documents

No	Doc. Id	Doc. Title	Date	Issue/ Revision/ Version
AD1	ESA/Contract No. 4000143397/23/I-NB CCI+ PHASE 2 - AIS	CCI+ PHASE 2 - NEW R&D ON CCI ECVS for AIS CCI	13.02.2024	NA
AD2	ESA-EOP-SC-AMT-2023-12 and its appendix 2	STATEMENT OF WORK, ESA EXPRESS PROCUREMENT – EXPRO CCI+ Phase 2 – Theme II – Antarctic Ice Sheet (AIS)	14.07.2023	1.2
AD3	ST-UL-ESA-AISCCI+-ATBD-001	ATBD for the Antarctic Ice Sheet CCI+ project of ESA's Climate Change Initiative Phase 1	09/03/2020	1.0

2 Surface Elevation Change

2.1 Introduction

Satellite altimetry provides estimates of ice sheet elevation changes through repeated measurements of ice sheet surface elevations. The technique has been employed to study both Greenland (Johanessen et al., 2005; Zwally et al., 2005; Zwally et al., 2011; Sørensen et al., 2011; Khvorostovsky 2012) and Antarctica (Wingham et al., 1998; Davis et al., 2005; Zwally et al., 2005), and has the distinct advantage of being able to resolve the detailed pattern of mass imbalance, with frequent (up to monthly) temporal sampling. Radar altimetry, in particular, provides the longest continuous observational record of all geodetic techniques (Wingham et al., 2009).

Altimeters using microwave frequencies are commonly referred to as radar altimetry. At these wavelengths the signal can penetrate cloud cover, making the measurements possible in all weather conditions. In addition, the use of microwaves enables measurements to be made independently from sunlight conditions. The satellites with altimeters on board are placed in repeat orbits (covering a region of up to 1 km on either side of a nominal ground track) enabling systematic monitoring of the Earth. Furthermore, satellite altimetry radars have been in continuous operation since 1991 and new missions are scheduled for the next decade. There is therefore the availability of long time series and as a consequence the possibility to monitor seasonal to inter-annual variations during the lifetime of these satellites.

In this CCI phase, we include new missions in our surface elevation change processing. Firstly SAR radar altimetry measurements from Sentinel-3A (from 2016) and Sentinel-3B (from 2018) and secondly laser altimetry measurements from IceSAT-2, which was launched in 2018. For all missions we include all new input product baselines, made available since the last phase of CCI.

Sentinel-3 mission data has recently (Q3 2023) been reprocessed by ESA as a land ice thematic product, making it finally suitable for inclusion in Antarctic surface elevation change processing. Prior to that, the available product measurement quality over the Antarctic margins was suboptimal due to low level ocean optimized Level-1 processing, removing parts of the signal over sloping surfaces.

ICESAT-2's laser altimeter (lidar) measures the air-snow interface whereas conventional radar altimeters are subject to penetration through the snow layer. Initially developed as a single mission surface elevation change product, we shall also report on the development of new FIRN correction, cross-calibration and merging algorithms necessary to merge the laser and radar altimetry into multi-mission products.

The specific objectives of this chapter are:

- to provide the theoretical basis of the algorithms that will be used to generate elevation changes grids from radar altimeter data;
- to assess the accuracy of these products; and
- to evaluate the range of applicability and the limitations of the derived data.

2.2 Review of scientific background

Radar altimeters provide a measure of the time, t_d, of a radio signal to travel from the emitting instrument, reach a target surface, and return/scatter back. The distance from the reflecting target to the radar is given by (Elachi, 1988):

$$r = \frac{ct_d}{2}$$ **Equation 2.1**

where c is the speed of light. The accuracy with which the distance is measured is given by

$$\Delta r = \frac{c}{2B}$$

Equation 2.2

where *B* specifies the signal bandwidth. The operating principle of an altimeter is shown in Figure 2.1 (a). Surface elevation h is calculated as the difference between the satellite altitude, *a*, and the measured range, *r*:

$$h = a - r$$

Equation 2.3

h is relative to the reference ellipsoid used for determining satellite altitude (see Figure 2.1 a). In addition to measuring range, the altimeter records a sample of the pulse echo return and estimates other parameters, including the magnitude of the return.

The side view representation in Figure 2.1 (b) shows the propagation of a single pulse along the beam of the antenna towards a horizontal and planar surface. The curved lines represent the pulse propagating and the temporal width between the curves is constant and equal to *ф*, the duration of the pulse length. A different visualization of the propagation (looking down on the scattering surface from the instrument position) is provided in Figure 2.1 b) (plane view). When the spherical wavefront first hits the surface at the instant time t0, the footprint is a point. The area illuminated by the pulse increases to a circular area until the trailing edge of the wavefront reaches the surface, at the instant time t1. The pulse-limited footprint is the maximum circular area defined as the radius of the leading edge of the pulse when the trailing edge of the pulse first hits the surface. As the pulse propagates, the circle transforms into rings of equal area (Fu and Cazenave, 2001). The figure shows also a typical return waveform. The power received begins to increase from the time when the wavefront hits the surface, t0, and continues to increase for the duration of the pulse. The waveform presents a linear leading edge corresponding to this initial interaction. At the times greater than the pulse duration, the area intercepted by the pulse remains constant with time. But, instead of remaining constant, the power of the reflected pulse actually decreases gradually with time according to the illumination pattern of the antenna. The mid-point of the leading edge corresponds to the range to the mean surface within the pulse-limited footprint.

Information about surface roughness is obtained from waveform analysis. When a pulse scatters from a surface, the returned echo has a shape reflecting the (statistical) properties of the surface. In the case of the ocean, where the surface is homogeneous, the height statistics are the main factors in determining the pulse shape. In the case of terrain, the surface composition varies across the antenna footprint and its statistical properties need to be taken into account. For a perfectly smooth surface, the echo is a mirror image of the incident pulse. If the surface has some roughness, some return occurs in the backscatter direction at slight off-vertical angles as the pulse footprint spreads on the surface. This results in a slight spread in time of the echo. If the surface is very rough, some of the energy is scattered when the radio pulse intercepts the peaks of the surface and more energy is scattered as the pulse intercepts areas at various heights of the surface. This leads to a larger multi-path spread of energy which results in noticeable rise in the echo leading edge. The rise is used to measure the surface roughness.

The propagation of the pulse with time, as described above, assumes the forming of the returns is by scattering from the surface only. However, it has been shown that ice sheet returns consist of a combination of surface and sub-surface volume scattering due to penetration of part of the radar signal through the snow surface (Ridley and Partington, 1988). Volume scattering mainly results from the presence of in-homogeneities in the host medium, like ice grains, air bubbles, and ice inclusions, whose size, shape, density, dielectric constant, and orientation affect the scattering. They cause a redistribution of the energy of the transmitted wave into other directions and results in a loss in the transmitted wave (Ulaby et el., 1982). Signal penetration is largest in the dry snow zone of the ice sheets and can exceed 5 m (Davis and Poznyak, 1993; Legresy and Remy, 1998).

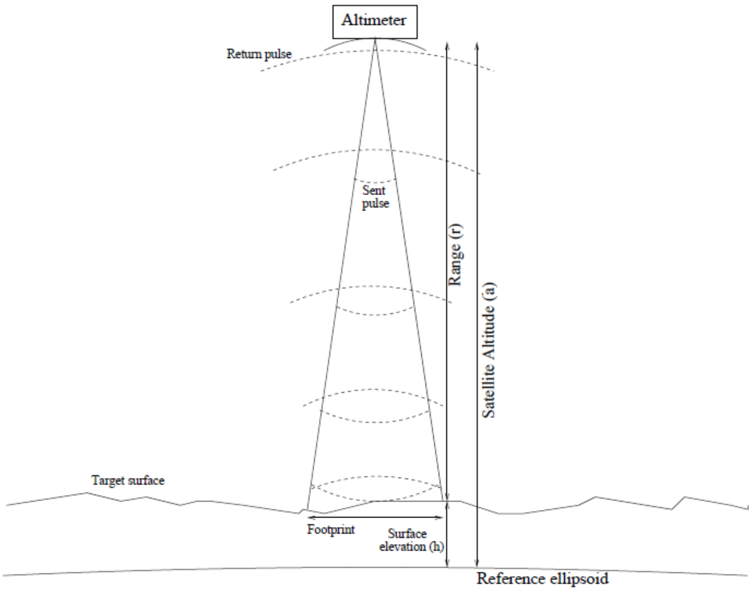

(a)

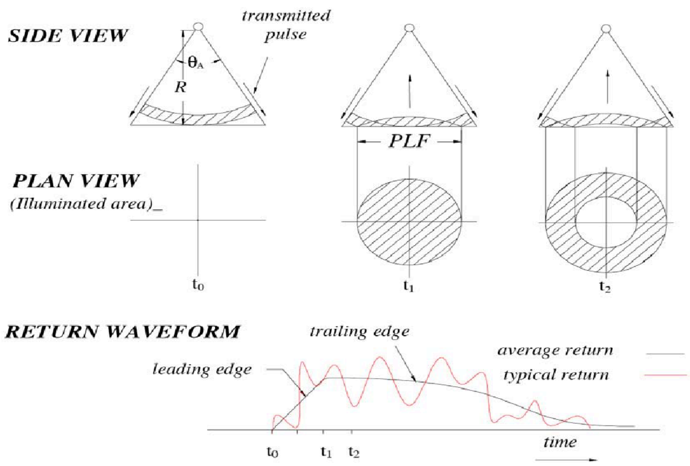

(b)

Figure 2.1: (a) Altimeter measurement principle; (b): The interaction of a radar altimeter pulse with a horizontal and planar surface, from its initial intersection (t_0), through the intersection of the descending edge of the wavefront with the surface (t_1), to the stage where the pulse begins to be attenuated by the antenna beam (t_2). The return is from surface only (Ridley and Partington, 1988).

Over ice sheet surfaces, the on-board tracker is generally unable to keep the leading edge of the waveform centred on the tracking point of the waveform window, and waveform retracking is to be applied to determine this offset. Several methods were developed for retracking ice sheet radar altimeter data (e.g. Bamber, 1994; Davis, 1997; Zwally and Brenner, 2001; Legresy et al., 2005). Retracking algorithms are based on defining the point where the waveform exceeds a certain percentage of the maximum power (threshold retrackers) or on functional fits to model waveform shape. All retrackers have their advantages and disadvantages, and selection of the retracker will affect taking of topography and volume scattering into account. Functional-fit retrackers more accurately produce individual elevation estimates, while threshold retrackers could be preferred for elevation change studies because they give more repeatable elevations.

The laser altimeter onboard ICESat-2 has a similar principle of operation to that of radar altimeters. The ICESat-2 green laser penetrates less into the snow surface and most of the returns come from the topmost surface due to its shorter wavelength. This can lead to return pulses being sensitive to short term ice sheet processes like snow drifting as well as atmospheric components like cloud cover and are also impacted by cloud cover and drifting snow (Markus et al., 2017). Hence they offer a more direct measure of ice sheet surface elevation changes which undergo high frequency changes.

2.3 Algorithms

The AIS CCI project performed extensive evaluation of several methods for deriving surface elevation change timeseries. These are documented in the AIS CCI ATBD (RD1). Only the algorithms that were used and will continue to be used in the CCI+ project, are described below. The general method of radar and laser altimetry processing used in the CCI products is described in *Ravinder et al*, 2024.

2.3.1 Plane fit

In an ideal case, ground-tracks or spot tracks for altimeter satellites in repeat-track orbits (like Envisat 2003-10, and ICESat) would repeat exactly so that elevations along the track at one time could be directly compared to elevations along the same track obtained at a different time. However, differences in the altimeter pointing angle and orbital perturbations will cause across-track differences, which should therefore be compensated for within the repeat track analysis. The unmeasured topography between near repeat-tracks also needs to be considered when comparing elevations from different tracks. Due to these considerations, instead of differencing individual tracks, the plane-fit method is used to model the surface change in individual geographical grid cells, using data from many tracks, both ascending and descending, simultaneously.

Recently, it has been found advisable for the algorithm to take more factors into account, as there may exist a correlation between backscatter power and surface elevation. Further, there may exist anisotropy in the measurements, i.e. a bias between measurements made during ascending passes and those made during descending passes. Terms to estimate the latter can be included in the surface model (McMillan *et al.* 2014). Elevation effects due to backscatter are removed by two extra steps that follow the surface modelling. Once the surface modelling step calculates the surface components of the modelled elevations, they are removed from the measured elevations to leave the temporal change and residual elements. A second modelling step determines the anisotropy of the backscatter component of the elevations, allowing removal of that component too. Finally, a linear fit correlates backscatter with elevation and is used to calculate a correction value applicable to a given time. The linear fit may only use data within a certain time period.

The plane fit algorithm (McMillan, *et al.*, 2014) is an adaption of the along track method which can be applied to satellites which operate in both short 27-35 day orbit repeat periods (such as the main operational periods of Envisat, ERS-1,2 and Sentinel-3A,B) and long 369 day repeat periods where measurements do not exactly repeat within monthly time scales such as CryoSat-2. The same algorithm is adapted to process ICESat-2 measurements with a 91 day repeat cycle. This method can also be used with orbit locations relocated to the true echo location such as with CryoSat SARin mode. Figure 2.2 shows how the layout of data points in an example grid cell varies with sensor and orbit pattern and how the measurements are gridded using along track and plane fit methods.

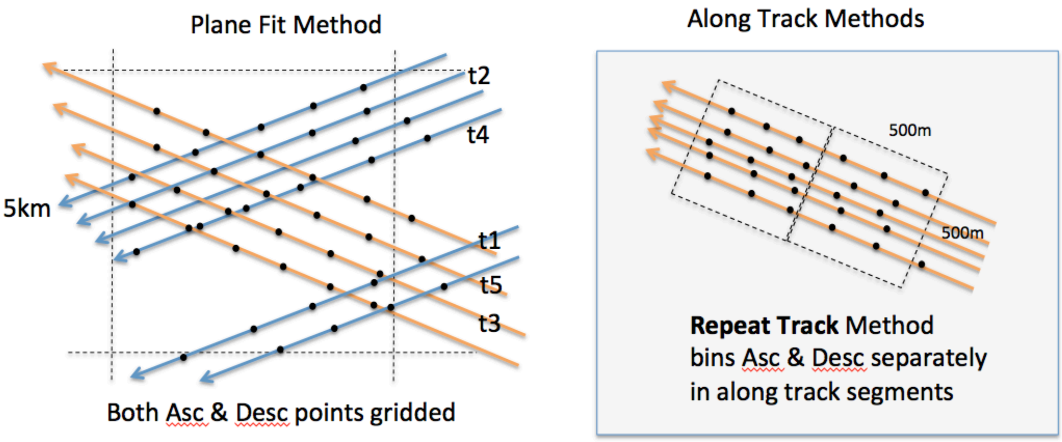

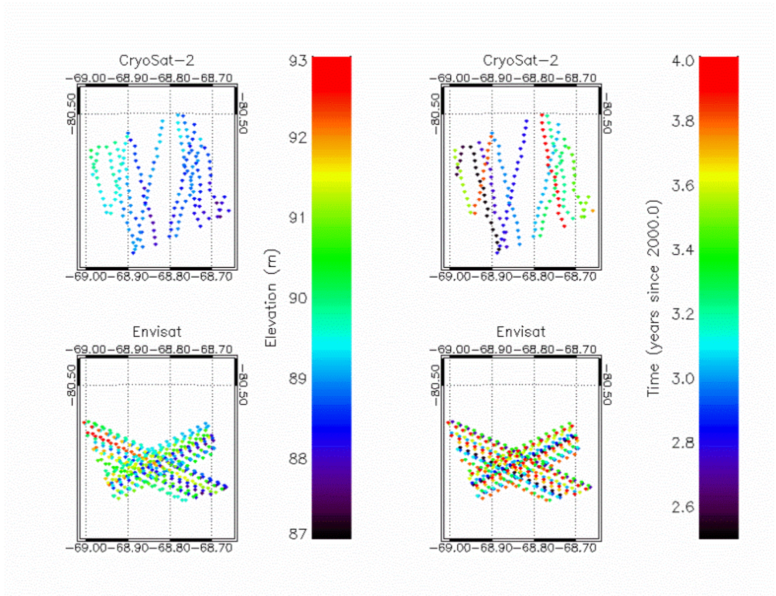

Figure 2.2: Example 5km by 5km grid cell on Filchner Ronne Ice Shelf, data points taken within an 18 month period. Locations slope-corrected. Measured elevations on left, timestamps on right.

The plane fit method grids both ascending and descending measurements in a regular polar stereographic grid instead of gridding separately along track. It derives a SEC estimate at the centre of each grid cell by applying a surface model to the measurements within that cell and has been shown in the CCI round robin experiments to perform as well or better than other along track methods for all missions (except Envisat's drifting phase from Oct 2010- Apr 2012, where special techniques are required for all methods) and hence was the primary along track method chosen for the Antarctic CCI. Another advantage of the plane fit method is that SEC results are produced on the same grid as the SEC output product and hence do not require re-gridding which can introduce an additional error and reduce accuracy.

Elevation changes are computed for each mission, for each geographical grid cell. Data falling within grid cells are only used to compute elevation changes if they contain 15 or more individual measurements. First a surface model is fitted to the cell data, using a Levenberg-Marquardt least squares fitting method. The model equation is

$$z(x, y, h) = z_m + a_0x + a_1y + a_2x^2 + a_3y^2 + a_4xy + a_5h + a_6t$$ **Equation 2.4**

where z is height, x is the polar stereographic easting coordinate, y is the polar stereographic northing coordinate, h is the satellite heading (set as binary), and t is the time of the elevation measurement in years. Measured heights more than two standard deviations from the modelled height are discarded, and this procedure is repeated until either no outliers or fewer than fifteen data points remained (in which case the results in the grid cell were not used).

A second model is then fitted to the slope- and satellite heading-corrected elevation anomalies emerging from each mission plane fit solution to remove residual, short-period fluctuations correlated with changes in backscattered power that arise in radar altimeter measurements over continental ice sheets (Wingham et al., 1998). This model is applied in a separate step to ensure that it does not interfere with the spatial and temporal elevation fit. It is again determined using a Levenberg-Marquardt least squares, with an equation of the form

$$p = a_0 + a_1 t + a_2 h$$ **Equation 2.5**

where p is the backscatter power, t is the time of the measurement in years, and h is the satellite heading. A time series of backscatter power is reconstructed using this model fit and the anomalies, and 5-year trends in $\frac{dp}{dz}$ were computed centred on the mid-point of each mission by matching the power and elevation anomaly time-series. These periods are chosen due to their relative stability in terms of orbit manoeuvres, outages and on-board changes. The fitting procedure is again iterated to remove outliers more than two standard deviations from the modelled value, either until there were none or more than three iterations had occurred (in which case the results were not used). As Sentinel-3A and B are recent missions, the power correction can only use two years of their data instead of five.

Finally the measurements are aggregated into 140-day epochs in each satellite mission. In each grid cell, the average residual height within each epoch is calculated using a resistant mean by discarding data more than two standard deviations from the median and compensating for the truncation with an approximation formula. The missions are then cross-calibrated to produce the final time series.

2.3.2 Cross-calibration

To produce continuous, multi-mission radar altimetry time-series of height change, biases have to be accounted for between missions. In all cases, the objective is to align ERS-2, Envisat, CryoSat-2, Sentinel-3A, Sentinel-3B timeseries. First, a model is defined for the shape of each time-series taking the form of a seasonal cycle imposed on a linear gradient. The model equation is

$$z = a_0 + a_1 t + a_2 \sin sin \left(2\pi t + a_3\right)$$ **Equation 2.6**

where z is the height change and t is the average time at each epoch in the series, in years. For each mission, the model coefficients are solved for using a Levenberg-Marquardt least-squares fit applied to sections of data that overlap as far as possible. . The lengths of each section vary due to the duration of the mission overlap and range from 1 to 3.5 years. For each overlapping pair of missions, the bias is then calculated as the median value of the difference between modelled height anomalies over a common, 2-year period, (e.g. figure 2.3, taken from Shepherd et al, 2019).

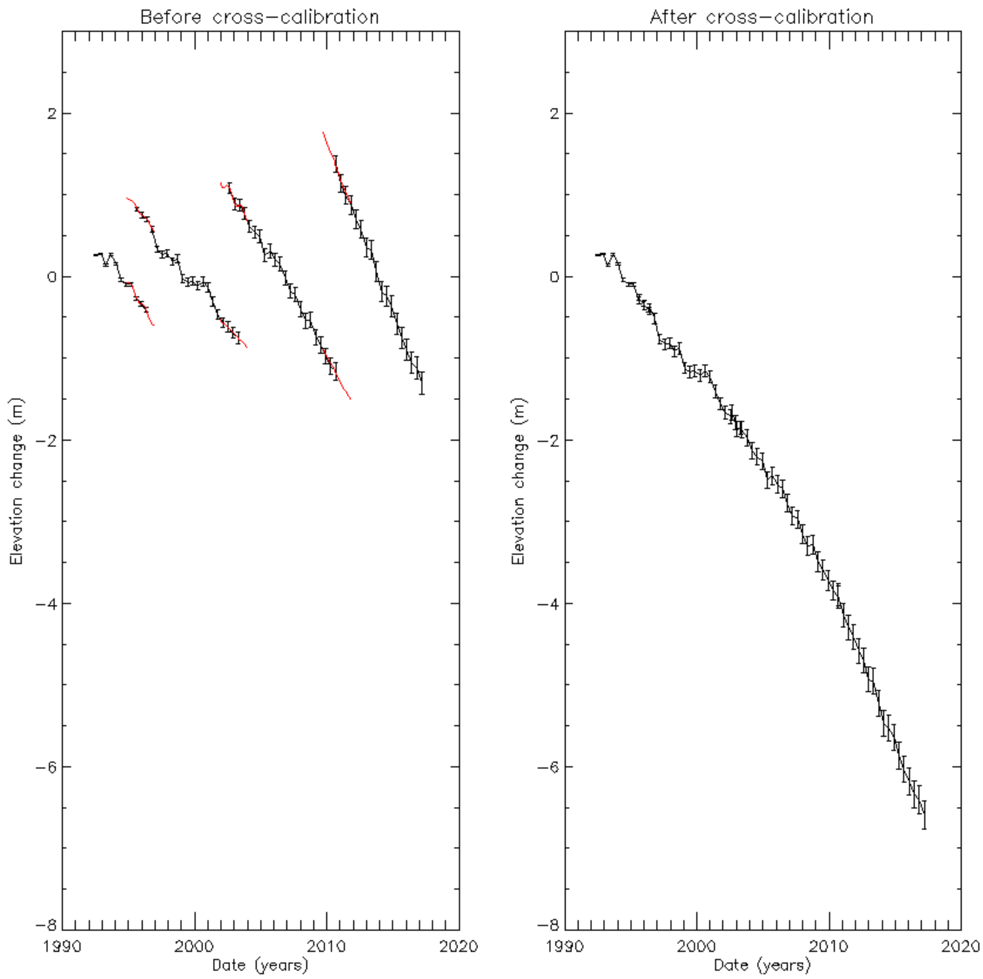

Figure 2.3: Example elevation trends computed from single mission time series (left) and the multi-mission ensemble (right) computed after adjusting for the bias arising at mission overlap periods (shown in red).

The biasing method can be applied to elevation changes within individual grid cells (pixel cross-calibration), and to averages computed over larger regions of interest (termed basin cross-calibration), including areas of ice dynamical imbalance, drainage basins, and ice sheets. The certainties of the bias corrections improve as the area of interest increases due to the volumes of data included in the model fits.

2.4 Input data and algorithm output

The raw input data is obtained from ESA or NASA Level-2 (thematic land ice) radar altimetry products from ERS-1/2, Envisat, CryoSat-2, Sentinel-3A/B and ICESat-2. Use of the new thematic land ice products (for example ESA CryoTEMPO Land Ice) provides the most up to date thematic level-2 processing to ice sheet elevation and related parameters.

Mission	**Thematic L2 Product**	**Version**
ERS-1	FDGR4ALT	v1.0
ERS-2	FDGR4ALT	v1.0
ENVISAT	FDGR4ALT	v1.0
CryoSat-2	CryoTEMPO LI	Baseline-C001
Sentinel-3A	ESA Thematic LI L2	BC005
Sentinel-3B	ESA Thematic LI L2	BC005
IceSAT-2	ATL-06	v006

In each case, the measurements used from the L2 products were time, slope-corrected geographic location (POCA), slope- and geophysically-corrected height, backscatter power and orbit heading (ascending or descending).

A correction is also applied to all missions' elevation measurements to account for the effects of post-glacial rebound, using the IJ05_R2 model (Ivins et al., 2013).

A generalised scheme for ingestion of from each radar altimeter is shown below (from L1b through to SEC product). The gridded outputs from each altimeter are then cross-calibrated to produce a single, similarly-gridded, output dataset.

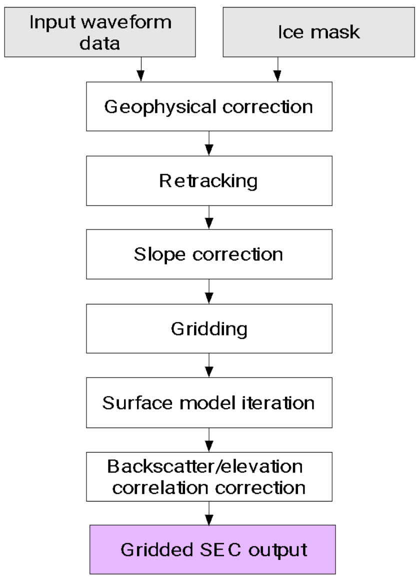

Figure 2.4. Schematic of the plane fit SEC processing line.

2.5 Accuracy and performance

For any given satellite mission, the uncertainty is estimated at each epoch of an elevation change (dz) time series as a combination of systematic and time-varying sources of error. Systematic errors are defined as those that may impact the long-term trend in elevation and are estimated from the standard error of the rate of surface elevation change (dz/dt) that is derived from each respective time series. Sources of systematic error may include spatially coherent changes in elevation that are not represented by the functional form of the surface model, such as short-lived accumulation events or changes driven by snowpack characteristics that are not accounted for by the empirical backscatter model (equation 2.5). It is unlikely that the assumed topography (plane, curved, digital elevation model (DEM), etc.) will perfectly represent the actual topography, and this introduces errors in the derived surface elevation change (SEC). In general, a simple topography applies better to the central, flat areas of the Antarctic ice sheet than the coastal areas characterized by a more complex topography. Therefore, the error is generally larger in areas with steeper surface slopes. Furthermore, the uncertainty on each individual elevation estimate is also slope dependent (Brenner et al., 2007).

For each time series, the systematic uncertainty is cumulatively summed at each epoch, so that the contribution from this component grows linearly with time. Additional, time varying uncertainty may arise due to errors that affect individual epochs and impinge on the ability to determine the regionally averaged elevation anomaly at that particular time. This term is influenced by factors such as measurement precision and non-uniform spatial sampling, and its influence is quantified based upon the dispersion of contributing measurements at each individual epoch. Specifically, for every epoch within any given time series, the regional average of the standard error of dz measurements within all contributing pixels is computed. In contrast to the systematic term, it is assumed that the time varying component is be temporally uncorrelated, and so at any given epoch all preceding epoch uncertainties are added, in quadrature.

One source of uncertainty which is not reflected by the modelling error estimate is the fact that radar signal penetrates into the snow, and that the penetration depth varies in both space and time, being a function of snow properties. Therefore, it is uncertain exactly how the radar derived SEC relates to the physical snow surface elevation change.

To estimate the cross-calibration uncertainty, the standard deviation of the differences between the modelled elevations from each successive pair of satellite missions is computed. This essentially measures the precision with which the two missions can be aligned, based upon the variance of the respective modelled elevations within the defined overlap period. The biasing uncertainty is set to zero for the first mission in the time series (ERS-1), as by definition no multi-mission adjustment is required, and then increases at each subsequent inter-mission boundary. Specifically, at each epoch the biasing uncertainties arising from all preceding inter-mission overlap periods are summed in quadrature. The total multi-mission uncertainty at each epoch is then computed by summing the single mission uncertainty (described above) and the biasing uncertainty in quadrature. Finally, the uncertainty on the multi-mission rate of elevation change is computed by dividing the total uncertainty accumulated at the end of the time series by the duration of the record, to ensure that all components of the uncertainty budget are taken into account within the resulting trend estimate.

Finally, the systematic and time-varying contributions are summed in quadrature, to determine an estimate of the overall elevation change uncertainty at each epoch.

In the preceding AIS CCI project, agreement between elevation change estimates obtained by the various along-track methods discussed and the crossover analysis demonstrated good performance capabilities of these methods. In another study (Horwath et al., 2012), elevation changes derived from the Envisat over the Antarctic Ice Sheet were compared with results of gravity changes from GRACE. In contrast to Thomas et al. (2008), the comparison showed a good agreement between linear trends and inter-annual variations that reflect surface mass balance changes. Although temporal changes of the surface properties are more pronounced in Greenland than in Antarctica, this result confirms the ability of radar altimetry to provide reasonable elevation change estimates.

In Antarctica the largest areas of known mass imbalance are over the continental glacial margins, and particularly of West Antarctica and the Antarctic Peninsula, mountainous areas of high slope and rough terrain. These are relatively poorly sampled by the tracking capabilities and orbital pattern of traditional pulse limited altimeter missions. However, CryoSat-2 with its interferometric SAR mode and improved spatial sampling of its orbit allows a dense survey of these regions. Comparison of elevation changes derived from CryoSat data using the plane fit method against results derived from airborne laser altimetry over the Amundsen Sea Sector of West Antarctica (McMillan, et al., 2014) where rates of ice thickness change are varied and large show that CryoSat measurements are in close agreement with these airborne observations. After adjusting for bias introduced by the airborne sampling pattern, the mean difference (31 cm yr−1) is smaller than the expected elevation fluctuation due to snowfall variability.

2.6 Capabilities and known limitations

The main advantages of the along track methods are an increased quantity and spatial distribution of elevation change measurements in comparison to the crossover method, again see the preceding AIS CCI project ATBD. They increase the SNR of the analysis and the spatial resolution of the measurements. The gridding allows the capture of local scale phenomena much better than the sparse crossover points. One disadvantage when using radar altimetry over ice sheets is that the radar-tracked surface changes with time; the penetration depth of the radar depends on the surface state. The measured height is then variable according to surface state variations or other volume echo intensity variations (linked to temperature changes impacting the medium’s absorption). A disadvantage of the plane fitting method is that the potential elevation change signal between the two repeat tracks is present in the reference plane.

The elevation-change timeseries survey the majority of the continental ice sheet area falling within the satellite orbital limits, but some places are omitted where gaps arise between the satellite ground tracks, where the altimeters fail to track rugged terrain, and where the mission cross calibration locally fails. This region includes some ice marginal areas due to the northwards broadening of ground track spacing. The largest single area of data omission is the region south of the satellite orbital limits, 88°S for CryoSat-2 and ICESat-2 and 81.5°S for the other missions.

2.7 References

Bamber, J.L. (1994). Ice sheet altimeter processing scheme, Int. J. Remote Sensing 15, 4, 925-938.

Brenner, A.C., J.P. DiMarzio, and H.J. Zwally, (2007). Precision and accuracy of satellite radar and laser altimeter data over the continental ice sheets, IEEE Trans. Geosci. Remote Sens. 45, 2, 321–331.

Cornford et al (2013), Adaptive mesh, finite volume modelling of marine ice sheets, Journal of Computational Physics, 232(1):529-549.

Davis, C.H. and A.C. Ferguson (2004). Elevation change of the Antarctic ice sheet, 1995-2000, from ERS-2 satellite radar altimetry, IEEE Trans. Geosci. Remote Sens. 42, 11, 2437–2445.

Davis, C.H. and V.I. Poznyak (1993). The depth of penetration in Antarctic Firn at 10 Ghz, IEEE Trans. Geosci. Remote Sens. 31, 5, 1107-1111.

Davis, C.H. (1997). A robust threshold retracking algorithm for measuring ice sheet surface elevation change from satellite radar altimeters, IEEE Trans. Geosci. Remote Sens, 35, 4, 974 – 979.

Davis, C.H., Y. Li, J.R. McConnell, M.M. Frey and E. Hanna (2005). Snowfall-driven growth in East Antarctic ice sheet mitigates recent sea-level rise, Science 308, 5730, 1898–1901.

Elachi, C. (1988). Spaceborne Radar Remote Sensing: Applications and Techniques, IEEE Press, New York.

ESA Climate Change Initiative, Essential Climate Variable, Antarctic Ice Sheet, Algorithm Theoretical Basis Document (2017) ST-UL-ESA-CCIAIS-ATBD-001v3

Ferguson, A.C., C.H. Davis and J.E. Cavanaugh (2004) An autoregressive model for analysis of ice sheet elevation change time series, IEEE Trans. Geosci. Remote Sens. 42, 11, 2426–2436.

Fu, L.L. and A. Cazenave (2001). Satellite Altimetry and Earth Sciences: A Handbook of Techniques and Applications. International Geophysics Series Vol. 69, Academic Press, San Diego, 457 pp.

Ewert, H, Groh, A and Dietrich, R. (2012). Volume and mass changes of the Greenland ce sheet inferred from ICESat and GRACE, Journal of Geodynamics, 59-61.

Horwath, M., B. Legresy, F. Remy, F. Blarel, and J. Lemoine (2012). Consistent patterns of Antarctic ice sheet interannual variations from ENVISAT radar altimetry and GRACE satellite gravimetry, Geophys. J. Int. 189, 863–876.

Howat, I. M., B.E. Smith, I. Joughin, and T.A. Scambos (2008). Rates of Southeast Greenland ice volume loss from combined ICESat and ASTER observations, Geophys. Res. Lett. 35, L17505.

Johannessen, O.M., K. Khvorostovsky, M.W. Miles and L.P. Bobylev (2005). Recent ice-sheet growth in the interior of Greenland, Science 310, 5750, 1013–1016.

Khvorostovsky, K. (2011). Merging and analysis of elevation time series over Greenland ice sheet from satellite radar altimetry, IEEE Trans. Geosc. Remote Sens. 50, 1, 23-36.

Legrésy B. and F. Rémy (1998). Using the temporal variability of satellite radar altimetric observations to map surface properties of the Antarctic ice sheet, J. Glaciol. 44, 147, 197–206..

Legrésy, B., F. Papa, F. Rémy, G. Vinay, M. Van den Bosh and O.Z. Zanife (2005). ENVISAT radar altimeter measurements over continental surfaces and ice caps using the ICE-2 retracking algorithm, Remote Sensing of Environment 95, 150−163.

Li, Y. and C.H. Davis (2006). Improved methods for analysis of decadal elevation change time series over Antarctica, IEEE Trans. Geosc. Remote Sens. 44, 10, 2687–2697.

Markus, T., Neumann, T., Martino, A., Abdalati, W., Brunt, K., Csatho, B., et al. (2017). The ice, cloud, and land elevation satellite-2 (ICESat-2): Science requirements, concept, and implementation. Remote Sensing of Environment, 190, 260–273.

McMillan, M., A. Shepherd, A. Sundal, K. Briggs, A. Muir, A. Ridout, A. Hogg and D. Wingham (2014). Increased ice losses from Antarctica detected by CryoSat-2, Geophys. Res. Lett. 41, 11, 3899-3905.

Moholdt, G., J.O. Hagen, T. Eiken and T.V. Schuler (2010a). Geometric changes and mass balance of the Austfonna ice cap, Svalbard, The Cryosphere 4, 21−34.

Moholdt, G., C. Nuth, J.O. Hagen and J. Kohler (2010b). Recent elevation changes of Svalbard glaciers derived from ICESat laser altimetry, Remote Sensing of Environment 114, 2756–2767.

Daniele Fantin, et al., (2015). Algorithm Theoretical Basis Document (ATBD) for CCI+ Phase 1 for the ice sheets CCI project of ESA's Climate Change Initiative, version 1.0

Pritchard, H. D., R.J. Arthern, D.G. Vaughan and L.A. Edwards (2009). Extensive dynamic thinning on the margins of the Greenland and Antarctic ice sheets, Nature 461, 971–975.

Ravinder. N, Shepherd. A, Otosaka. I, Muir. A, Slater. T, Gilbert. L, Greenland Ice Sheet Elevation Change From CryoSat-2 and ICESat-2, GRL, Dec 2024.

REAPER REA-UG-PHB-7003 Product Handbook Issue: 2.2 Date: 12/05/2014

Ridley, J. K. and K. C. Partington (1998). A model of satellite radar altimeter return from ice sheets, Int. J. Remote Sensing 9, 4, 601424.

Shepherd et al (2019), Trends in Antarcic Ice Sheet Elevation and Mass, GRL 46 (14) 8174-8183

Slobbe, D.C., R.C. Lindenbergh and P. Ditmar (2008). Estimation of volume change rates of Greenland's ice sheet from ICESat data using overlapping footprints, Remote Sensing of Environment 112, 4204–4213.

Sørensen, L.S., S.B. Simonsen, K. Nielsen, P. Lucas-Picher, G. Spada, G. Adalgeirsdottir, R. Forsberg and C.S. Hvidberg, (2011). Mass balance of the Greenland ice sheet (2003–2008) from ICESat data – the impact of interpolation, sampling and firn density, The Cryosphere 5, 173–186.

Thomas, R.H., C.H. Davis, E. Frederick, W. Krabill, Y. Li, S. Manizade and C. Martin (2008). A comparison of Greenland ice sheet volume changes derived from altimetry measurements, J. Glaciol. 54, 185, 203–212.

Ulaby, F. T., R.K. Moore and A.K. Fung (1982). Microwave remote sensing: active and passive, Addison-Wesley Publishing Company, London.

Whitehouse, P. (2009). . 2009;105, http://www.skb.se/upload/publications/pdf/TR-09-11.pdf.

Wingham, D.J., A.L. Ridout, R. Scharroo, R.J. Arthern and C.K. Shum (1998). Antarctic elevation change from 1992 to 1996, Science 282, 5388, 456–458.

Wingham, D.J., D.W. Wallis and A. Shepherd. (2009). Spatial and temporal evolution of Pine Island Glacier thinning, 1995-2006, Geophys. Res. Lett. 36,

Zlotnicki, V., L.L. Fu and W. Patzert. (1989) Seasonal Variability in Global Sea Level Observed with Geosat Altimetry, J. Geophys. Res. 94, C12, 17959-17969,

Zwally, H.J. and A.C. Brenner (2001). Ice sheet dynamics and mass balance, In: Fu, L.L. and A. Cazanave (eds.) Satellite altimetry and earth sciences, New York, Academic Press Inc., 351–369.

Zwally,H. J.,R. A. BindschadlerA,. C. Brenner,T. V. Martin,and R. H. Thomas. (1983). Surface elevation contours of Greenland and Antarcticice sheets,J. Geophys.Res., Vol 88, No. C3, pages 1589-1596

Zwally, H.J. (1989). Growth of Greenland ice sheet: interpretation, Science 246, 4937, 1589–1591.

Zwally, H.J., J. Li, A.C. Brenner, M. Beckley, H.G. Cornejo, J. DiMarzio, M.B. Giovinetto, T. Neumann, J. Robbins, J.L. Saba, D. Yi and W. Wang. (2011) Greenland ice sheet mass balance: distribution of increased mass loss with climate warming; 2003- 07 versus 1992–2002, J. Glaciol. 57, 201, 88–102.

Zwally, H.J., M.B. Giovinetto, J. Li, H.G. Cornejo, M.A. Beckley, A.C. Brenner, J.L. Saba & D. Yi (2005) Mass changes of the Greenland and Antarctic ice sheets and shelves and contributions to sea-level rise: 1992–2002, J. Glaciol. 51, 175, 509–527.

3 Ice Velocity and Ice Velocity Change

3.1 Introduction

In Antarctic Ice Sheet CCI+ the developments and further production for Ice Velocity (IV) build on the achievements of Antarctic Ice Sheet CCI (AIS CCI) Phase 1 and Phase 2 (2012-18) and CCI+ Phase 1. The major technical advancements emerging from AIS CCI were the development and implementation of an automatic system for the generation of ice velocity maps from repeat pass Copernicus Sentinel-1 (S1) Synthetic Aperture Radar (SAR) using offset tracking (OT). The annual velocity maps and unprecedentedly dense IV time series of outlet glaciers provide essential information for studying temporal fluctuations and long-term trends and provide key input for ice dynamic and climate modelling. The production of the annual maps is continued within the Copernicus Climate Change (C3S) service on ice sheets.

In Antarctic Ice Sheet CCI+ the key novel development for the ice velocity (IV) retrieval algorithm in Phase 1 of the project was the implementation of an Ice Velocity Tidal Correction Module (IV-TCM) in the IV processing chain. The IV-TCM corrects the ice velocity on ice shelves and floating extensions of outlet glaciers (e.g. ice tongues) for tidally induced vertical motion. In Phase 2 of the project the focus of development is on the inclusion of SAOCOM SAR data in the processing chain, testing of InSAR-augmented IV retrieval and preparation for a new product on Ice Velocity Change (IVC). Demonstration products showcasing ice velocity change across various regions will be produced.

This chapter provides the Algorithm Theoretical Basis for IV, building on the ATBD of AIS CCI (RD1) and AIS CCI+ Phase 1, and provides an overview, description, and update of the scientific background, the IV retrieval algorithms, input, and output data, expected accuracy and performance, and capabilities and known limitations. The Sentinel-1 processing line has been amended to accommodate SAOCOM data as well as the combination of SAOCOM and Sentinel-1 (OT and InSAR).

3.2 Review of scientific background

The principal method for generating velocity fields on glacier and ice sheet surfaces is Offset Tracking (OT). OT refers to several related methods that include amplitude tracking or feature tracking, coherence tracking and speckle tracking. Feature tracking uses cross-correlation of image patches to find the displacement of surface features such as crevasses or rifts and edges, that move with the same speed as the ice and are identifiable on two co-registered amplitude images, and subsequently ice flow velocity. In coherence tracking (SAR only), the offset which maximises the interferometric coherence within a certain window size is determined and used to derive the ice velocity. Speckle tracking (SAR only) uses the cross-correlation function of radar speckle patterns, rather than visible features, to derive ice flow velocity.

Spaceborne methods for measuring ice velocity have focused primarily on the above mentioned methods applied to both optical and SAR sensors (Joughin et al, 2010; Nagler et al, 2015; Mouginot et al, 2017; Joughin et al, 2018). The use of SAR data has several advantages over optical imagery, including the ability to observe through cloud cover and during the polar night. Another advantage is that penetration of radar waves into the upper snow layers can reveal shallow subsurface or snow-covered features that can be successfully tracked but are usually hidden in optical imagery. Also, there is a stronger contrast between different types of ice (e.g. sea ice and ice shelves) in SAR imagery that are difficult to distinguish in optical imagery, allowing ice shelf edges to be tracked more easily.

OT has been extensively applied to the Greenland and Antarctic Ice Sheets and has proven to be efficient for large-scale continuous monitoring (Nagler et al, 2015; Joughin et al, 2018). However, SAR offset-tracking methods are amplitude-based and do not exploit the full information provided by SAR images. Their accuracy is primarily controlled by the spatial resolution (i.e., pixel posting) of the sensor and reaches at best some meters per year. In contrast, differential SAR interferometry (InSAR) can reach a precision of one to two orders of magnitude better than OT. Even though InSAR has proved efficient for ice monitoring, it has been scarcely used for large scale or continuous monitoring of ice sheets. InSAR requires measurements from crossing ascending and descending orbits to determine the different components of the velocity vector (Joughin, 1998; Gray, 2011). In addition, the application of InSAR also requires a good level of coherence between repeat image pairs to generate suitable interferograms. The Greenland Ice Sheet is subject to highly variable meteorological conditions, resulting in rapid temporal decorrelation of the radar signal phase impairing the comprehensive application of InSAR. For this reason, InSAR is in general applied to complement OT measurements (Joughin, 2002; Rignot et al, 2011; Mouginot et al, 2012). OT is less sensitive or insensitive to temporal decorrelation of the radar phase signal, albeit at a lower accuracy of velocity. In areas with distinct and stable surface features, as common on mountain glaciers and outlet glaciers of ice sheets, coherence of the repeat-pass SAR data is not required because the cross-correlation of image-templates is based on the amplitude signal.

Sentinel-1 has significantly increased the SAR coverage in the polar regions, with routine 6- and 12-day coverage of the GIS margins and peripheral glaciers as well as smaller Arctic ice caps and glaciers. Before the launch of Sentinel-1, crossing orbit SAR data were not systematically acquired and not always with a satisfactory temporal baseline. The unprecedented data set provided by the Sentinel-1 satellites opened the possibility to improve IV measurements over Greenland by applying InSAR in a more systematic fashion. Nevertheless, some glacier areas are covered by only one single Sentinel-1 track, making it impossible to derive the full velocity vector from InSAR only and reducing the applicability of InSAR for ice velocity retrieval. However, if the flow direction is known and assumed constant, InSAR measurements can be used to retrieve the magnitude of the velocity vector. In contrast to InSAR, OT can derive velocity vector components from a single acquisition geometry. Even though OT is much less accurate than InSAR when applied to a single pair of images, it reaches a satisfactory accuracy when stacking measurements over longer periods. To improve existing maps and maximize the synergy of InSAR and OT, it is possible to combine the flow direction derived from OT with the InSAR line-of-sight (LoS) velocity measurements, assuming stability of the flowlines over time (Nagler et al., 2022). With this approach, the velocity field can be determined, wherever single- or multi-track InSAR measurements are available, except on the ice divide where the flow vector is null.

Recently, the loss of Sentinel-1B has hampered the application of InSAR due to the reduced repeat-pass period from 6 to 12 days as well as the reduced coverage of crossing-orbits pairs. 8-day repeat-pass L-Band SAR data over the Antarctic Peninsula are since 2021 also acquired by SAOCOM A/B SAR mission as a background mission (i.e. without systematic acquisition plan) and is tested here as a possible way to fill in this gap. The prime payload of the dual satellite constellation is an L-band polarimetric SAR instrument, managed and operated by CONAE (Comisión Nacional de Actividades Espaciales - Argentina's Space Agency). By using L-Band SAR data the use of the InSAR method can be extended to cover faster moving areas than possible with C-band (Sentinel-1). L-band data have a reduced fringe frequency in shear zones and fast-moving areas, enabling more reliable phase unwrapping so that the InSAR method can also be applied in zones where Sentinel-1 data decorrelate. Additionally, the L-band signal coherence is less affected by variable surface conditions than C-band. Consequently, further improvement for ice velocity monitoring can be expected from the synergy of C-band and L-band InSAR data, as rendered possible by combining Sentinel-1 and SAOCOM A/B. Using SAOCOM data we focus the work in Phase 2 of AIS CCI+ on the developments of methods for combining L- and C-Band interferometric data for ice velocity monitoring using both InSAR and OT.

3.3 Algorithms

3.3.1 SAR Offset Tracking

Figure 3.1 shows the high-level flow chart for offset tracking to retrieve maps of ice sheet surface velocity using repeat-pass SAR images, as implemented in ENVEO's SAR processing system. The generalised processing line for offset-tracking could be readily adapted to accommodate also SAOCOM data. The software contains three main modules.

Within the IV module SAR data and orbit data are imported into the system, SAR images are co-registered and velocity maps are generated for pairs of repeat pass data of the same track. The importer imports the repeat-pass SAR data and corresponding metadata describing SAR, focussing, orbit and attitude information. The coregistration performs the alignment of the second (slave) image with the first (master) image, whereby the master image defines the geometry.

Geometric DEM-assisted coregistration is applied, computing for each pixel of the master image acquisition the corresponding pixel in the slave scene and storing the relative shift in the shiftmap file. In the case of accurate orbit and attitude information, as provided by TerraSAR-X, TanDEM-X and Sentinel-1, this co-registration step is sufficient for proceeding with the ice velocity retrieval. For older SAR systems or systems with less accurate orbits (e.g. SAOCOM), in addition an iterative cross-correlation over stable terrain or OT assisted co-registration (using a long-term averaged map) is needed in order to improve the estimate of the local shift in range and azimuth for the slave relative to the master image. The IV generation performs advanced iterative OT to generate detailed displacement maps in SAR geometry. The tracks are geocoded into the common map projection of the output grid, providing observations of slant range displacement and azimuth for each track separately. The local incidence and heading angle are calculated using the annotated image and orbit parameters and a DEM as input.

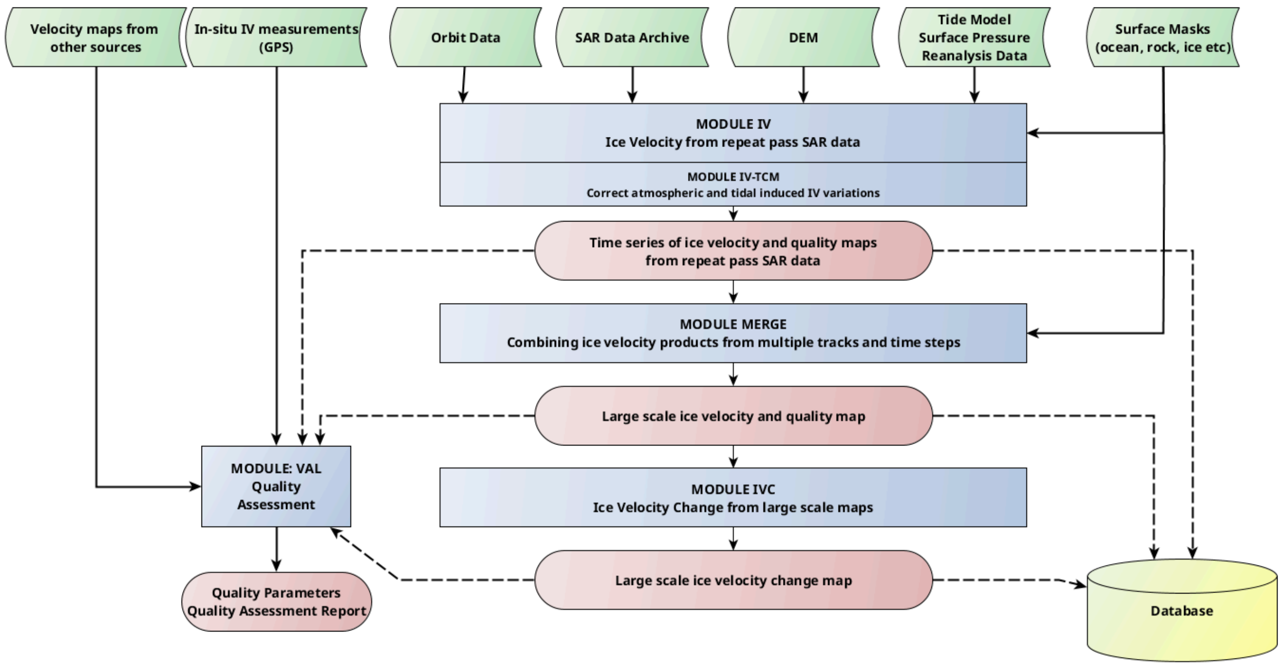

Figure 3.1: High-level flow chart of the ENVEO ESP 2.1 IV processing system. Green: input data, blue: processing modules, red: (intermediate) products, yellow: database.

The Merge module combines IV products from different tracks and image pairs (with various repeat intervals) over a specified time span (i.e. 1 year) to generate a regional ice velocity map, applying a weighted average approach. The combination of displacement observations of multiple tracks applies a weighted least squares model to fit the multiple observed displacements according to:

$$y = Ax + \epsilon$$

where x is the horizontal velocity vector (in local Easting/Northing coordinates), y is a vector with the observed velocities (in slant range/azimuth), A is the matrix projecting the horizontal velocity to slant range/azimuth geometry, and ϵ is a noise vector.

Lastly the Validation module facilitates quality assessment of the IV products, by automating various standard validation tests, including internal consistency checks and intercomparisons with independent data sets (e.g. in-situ GPS, or other published velocity maps).

3.3.2 SAR Interferometry

The interferometric phase difference between two SAR images acquired at separate times is the sum of multiple components:

$$\phi = \phi_{flat} + \phi_{topo} + \phi_{displ} + \phi_{atm} + \phi_{iono}$$

where ϕ_{flat} is the flat-earth phase, ϕ_{topo} is the topographic phase, ϕ_{displ} is the phase due to ground displacement along the sensor line-of-sight (LOS), ϕ_{atm} is the atmospheric phase and ϕ_{iono} is the ionospheric phase. To estimate ice velocity, the displacement phase component must be isolated. This means that DInSAR processing includes removal of flat-earth and topography. Under the assumption that the atmosphere and the ionosphere are in a similar state for both acquisitions, the atmospheric and ionospheric components may be neglected.

The interferometric phase is computed as the argument of the product of the master image with the complex conjugate of the slave image. The result is a wrapped version of the absolute phase, with values ranging between and . The interferogram must be unwrapped to retrieve the absolute phase. However, phase unwrapping algorithms usually estimate the unwrapped phase of a pixel with respect to the phase of its neighbours. As a result, the unwrapped phase is shifted by an unknown amount with respect to the absolute phase. For this reason, the unwrapped phase must be further calibrated: the knowledge of points with zero velocity is used to determine the phase shift to be applied.

Once calibrated, the absolute phase must be converted into LOS velocity: LOS displacement is obtained by applying a $\lambda/4\pi$ conversion factor, with λ being the radar wavelength, and the velocity is calculated as the displacement per day, knowing the temporal baseline of the interferometric couple. When interferometric processing is applied to a single geometry (i.e., to a given track, ascending or descending, with given heading and incidence angles), it only measures the displacement projected onto the line-of-sight. For calculating the 3-D velocity, LOS measurements from different geometries must be merged.

Because interferometric measurements are prone to decorrelation, interferometry can only perform efficiently over ice bodies with stable conditions between the acquisitions: no melting, same type of snow surface, etc. Moreover, interferometry performs better on slow-moving areas: indeed, ice velocity can reach very large values (e.g., meters per day) causing important displacements even over a few days. Such displacements cannot be measured with interferometry as they result in aliased fringes in the interferogram that cannot be unwrapped.

The high-level processing line for InSAR is pictured in Figure 3.2. This processing line is originally designed for Sentinel-1 TOPSAR acquisitions (cf. IW – Interferometric Wide mode), but it can be easily modified to suit other sensors and acquisition modes. Adaptation of the processing line for SAOCOM data focuses on handling large baselines and automatization of co-registering. SAOCOM data, by combining orbital data, a DEM and refinement using local matching, which is needed due to the reduced quality of the orbital state vectors.

In S1 TOPSAR mode, the antenna is sequentially steered from the aft to the fore, so that the ground is not continuously scanned. The imaged area is scanned as 3 sub-swaths (or 5 in EW – Extended Wide mode), which are divided into slightly overlapping bursts. The interferometric processing, including co-registration, interferogram generation, phase flattening and topography removal is performed on each burst separately. The burst interferograms are then mosaicked at the debursting step.

The subsequent processing is performed at the deburst level. Once the interferogram is generated, the phase must be unwrapped and calibrated. Afterwards, it can be converted into LOS velocity. In ENVEO implementation, the LOS velocity is also projected onto the horizontal plane. Images of horizontally projected LOS velocity are produced for different tracks and dates, and they are all geocoded on a common projection grid. Finally, these maps are used for inverting the system described below and for estimating the components of the horizontal velocity. The final product is a measurement of the east-west and north-south component.

In case of another acquisition mode than TOPSAR (e.g., Stripmap mode as used for SAOCOM), the processing line is similar but the debursting step can be skipped as we are directly working with large-scale images. A short description of each module is provided below.

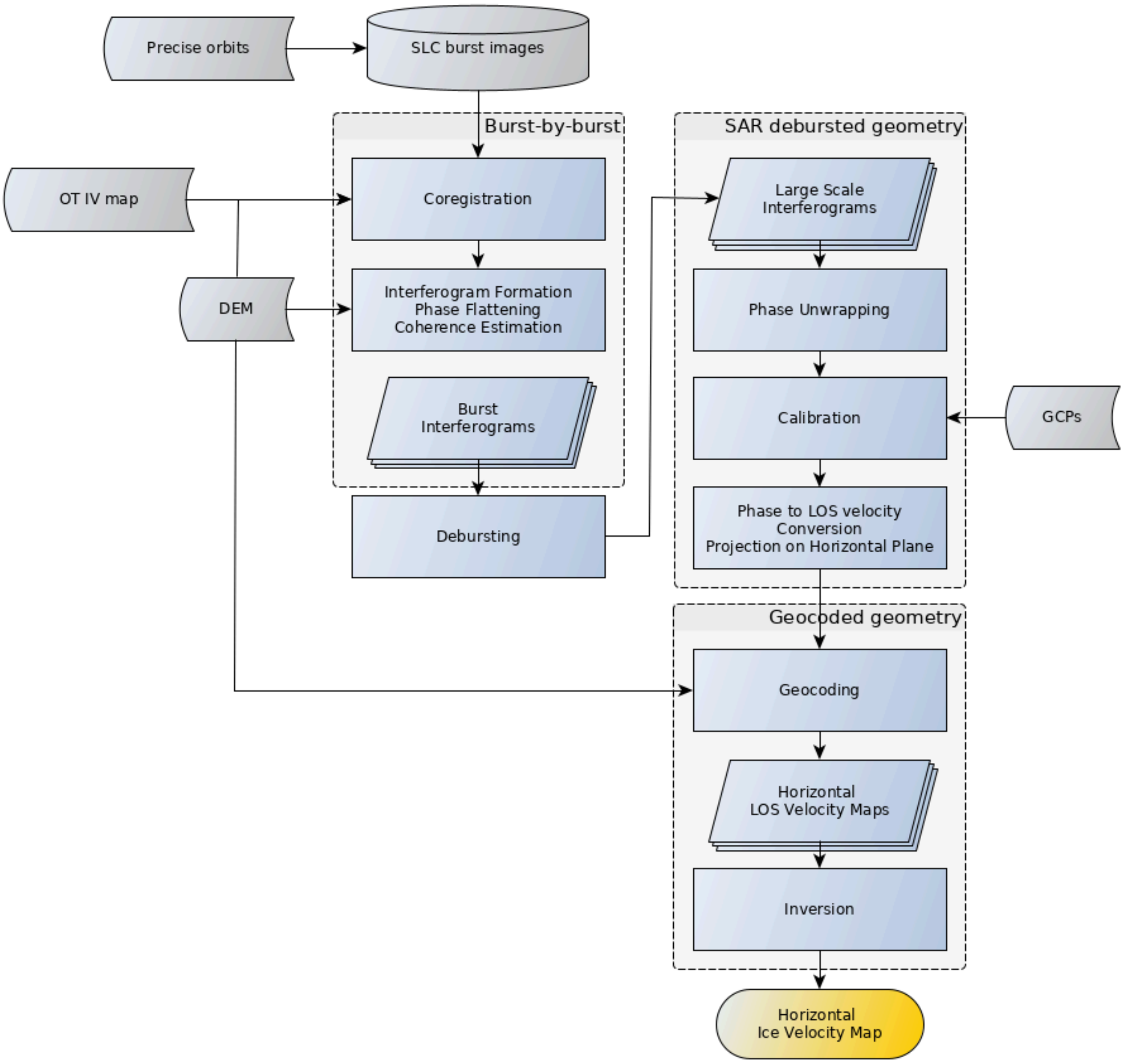

Figure 3.2: Interferometry processing for ice velocity (IV) map generation. The flowline is dedicated to Sentinel-1 TOPSAR acquisitions. SLC – Single-Look Complex. OT – Offset Tracking. LOS – Line-of-sight. GCP – Ground Control Point. For SAOCOM SM the flowline is similar but the debursting step is not necessary.

- **Coregistration:** For S1 co-registration is performed at the burst level, but is otherwise similar as for SAOCOM. Precise orbits and a Digital Elevation Model (DEM) of the area are used to determine the shifts between the master and slave geometry. In S1 TOPSAR mode, because of the steering of the antenna, the line-of-sight changes from one burst to the other at the overlapping area. In case of motion in the azimuth direction, the varying line-of-sight introduces phase discontinuities at burst overlap. We correct this effect by accounting for the average ice motion: using the IV map from Offset Tracking, we update the co-registration map with the local displacements between the master and slave acquisition dates. The co-registration module also includes the resampling step. For Sentinel-1 data, the steering of the antenna introduces a Doppler frequency variation in the azimuth direction. Therefore, the co-registration of Sentinel-1 images includes de-ramping and re-ramping of complex images in the azimuth direction respectively before and after interpolation.

- **Interferogram formation**: the interferometric phase is calculated for each master-slave burst pair. The flat-earth phase is estimated and removed. The topographic phase is estimated from an external DEM and subtracted from the interferogram. The output is the wrapped displacement phase.
- **Debursting:** burst interferograms are mosaicked together using the range and azimuth time information of each pixel. Additional smoothing at the burst overlap can be performed to remove phase jumps due to changing orientation of the line-of-sight. These phase jumps are already significantly reduced by accounting for ice motion at the co-registration step. This step is only needed for S1 TOPS mode data and not for SAOCOM SM data.
- **Phase unwrapping:** phase unwrapping of very large interferograms can either be handled with SNAPHU, applying a tiling strategy (Chen and Zebker, 2002), or with an iterative least-square phase unwrapping.
- **Calibration:** calibration is usually performed by using zero-velocity ground control points (GCPs). However, zero velocity GCPs are not always available for all tracks covering the Greenland Ice Sheet. Therefore, we select low velocity as GCPs and perform calibration by adjusting their phase to the average velocity provided by the IV map from OT. For this purpose, the IV map must be projected into SAR geometry, multiplied by the temporal baseline to yield the displacement, and converted into phase. A low order polynomial function is fitted to the difference between the IV phase from OT and InSAR of slow-moving points. If the polynomial order is 0, then the calibration function consists in a simple constant shift. If the order is equal to 1 in azimuth and range directions, then the calibration function consists in a plane and accounts for possible orbits errors in the phase.
- **Phase-to-velocity conversion:** the calibrated absolute phase is converted into LOS velocity (i.e., displacement per day) by applying pixel wise the conversion factor $\frac{\lambda}{4\pi\Delta t}$, with being the radar wavelength and the temporal baseline (usually provided in days). At this stage, the LOS velocity is further projected onto the horizontal plane. Projection onto the horizontal plane is obtained by dividing LOS velocity by the factor , where is the local incidence angle. Projection onto horizontal eases the final inversion, as all velocity vectors are already on a common plane and the system to be inverted only needs to account for heading angles.
- **Geocoding:** horizontally projected LOS velocity from all dates and tracks are geocoded on a common projection grid.
- **Inversion:** this step is meant to determine average horizontal velocity components. Provided that velocity measurements from at least two different geometries (i.e., two different heading angles) are available for a given point, the east-west and north-south velocity components can be determined. For this purpose, the system to be inverted is:

$$V_{LOS}=AV \quad \textbf{(3.2)}$$

where is the N-dimensional vector of the measured LOS velocities projected on the horizontal plane, A is the matrix with dimensions N x 2 projecting the horizontal velocity on the LOS and V is the 2-dimensional vector of horizontal velocity components. Let us consider N horizontally projected LOS velocity measurements . The index refers to the geometry of acquisition and the corresponding heading angle . The system can be explicitly written as:

$$\left[v^H_{los_1}\, v^H_{los_2} \quad v^H_{los_N}\right]=\left[\cos\cos\phi_1 \sin\sin\phi_1 \cos\cos\phi_2 \sin\sin\phi_2 \quad \cos\cos\phi_N \sin\sin\phi_N\right]\left[v_E\, v_N\right] \quad \textbf{(3.3)}$$

Where v_E and v_N are respectively the east and north components of the horizontal surface velocity. These components can be determined only where data with crossing orbits (e.g. ascending SAOCOM – descending Sentinel-1) are available.

3.3.3 Combined InSAR and OT

The combined approach of InSAR and OT flow direction is described in Fig. 3.3. In this flowchart, the InSAR processing corresponds to the interferometric processing for ice velocity retrieval described in section 3.3.2. In parallel to the interferometric processing, the flow direction is derived from the OT multiannual velocity map. The flow direction is computed as the angle between the velocity vector and the east direction.

The line-of-sight (LOS) velocity maps resulting from the interferometric processing and the OT derived flow direction map are combined in the inversion process, which consists of a weighted least squares linear regression. Since the LOS velocity data points are the projected measurements of the velocity vector, they have a linear dependence on the projection coefficients and this linear dependence has a slope corresponding to the velocity magnitude. The projection coefficients are defined by the flow direction and the InSAR geometry (incidence and heading angles). Therefore, the inversion process enables estimating the velocity magnitude, which is finally projected on the x and y direction of the ice flow for computing the x-, y- and z-components of the velocity field.

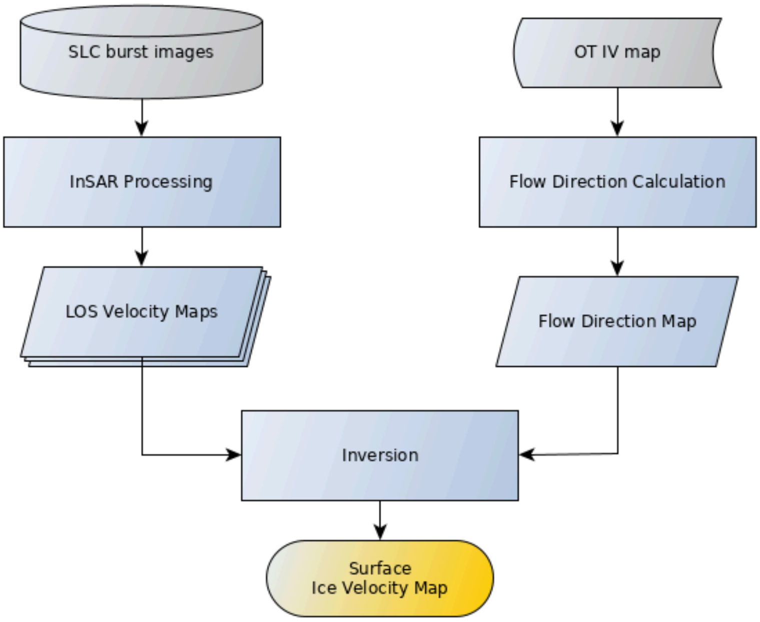

Figure 3.3: Combined approach of SAR interferometry and offset-tracking for ice velocity retrieval.

3.3.4 Ice Velocity Change

In Phase 2 of the project, the ECV product portfolio will be expanded to include Ice Velocity Change (IVC). IVC is a fundamental ice sheet parameter which is key to detecting and investigating dynamic instabilities and to identify and distinguish short term fluctuations from longer term trends that may be induced by climatic and/or oceanographic changes. Currently under development, the IVC will be built as a separate module integrated into the overall ice velocity processing line. This module aims to produce large/regional scale ice velocity change maps using the output of the MERGE IV as input. In the first stage IVC is derived by differencing monthly and/or annually averaged regional IV maps. In a second stage we will also investigate the possibility of calculating a deviation from a long-term mean, which could be a moving 5-year averaged IV map. Different options can be applied:

- Annual change compared to previous year
- Monthly change compared to previous month

- Monthly change compared to the same month of previous year.

3.4 Input data and algorithm output

3.4.1 Input Data

Input data for IV products generated in CCI+ Phase 2 consists of both Sentinel-1 and SAOCOM SLC images. Because SAOCOM has a much larger orbital tube and generally no burst synchronisation in TOPSAR mode we use SAOCOM StripMap (SM) data. Given that ice motion can already cause very large displacements over short intervals, in general only short temporal baselines are selected (6 and 12 days for Sentinel-1, 8 or 16 days for SAOCOM), but for SAOCOM we also test larger temporal baselines up to 32 days. Moreover, the changing state of the ice during the melting season can cause decorrelation and prevent InSAR measurements. Therefore, we mainly focus on the winter season, but this is primarily dictated by the availability of suitable repeat-pass SAOCOM data which is sparse in Antarctica to date.

For Sentinel-1 TOPSAR acquisition, the input data are pairs of master and slave bursts in SLC format. In best cases, Sentinel-1 has a revisit cycle of 6 days (currently 12 days). Sentinel-1 IW and EW TOPS Mode SLC Products, as provided by ESA, consist of 3 or 5 sub-swaths, each consisting of a series of bursts, each burst has been processed as a separate SLC image. By importing Sentinel-1 SLC IW/EW SLC products into the software system each burst is extracted separately and the corresponding metadata information is stored in separate files. We take care to assign correct azimuth timing and slant-range timing for each burst, which is needed for debursting and for co-registering corresponding bursts of repeat pass acquisitions. Within the IV processor software an imported burst can be treated the same way as a frame of Stripmap Mode SAR data (e.g. SAOCOM), except for the phase de-ramping needed during the resampling step.

The SAOCOM-1 SAR mission is composed of two satellites (SAOCOM-1A and 1B) with L-band polarimetric SAR launched in 2018 and 2020 respectively. The mission is managed and operated by the Comisión Nacional de Actividades Espaciales (CONAE). SAOCOM provides L-Band SAR data over glaciers and ice sheets as a background mission, without systematic acquisition plan, and has a revisit time of 16 days (with 1 satellite) and 8 days (with the constellation). There are two main operational modes, Stripmap (SM) and TopSAR, operating with 9 beam modes (S1-S9) with incident angles ranging from 20-50 degrees.

Precise orbits of Sentinel-1 acquisitions are provided by ESA as independent products. These orbits have 5 cm accuracy in the along-track, across-track and vertical directions and are available 20 days after the acquisition. Orbits for SAOCOM are provided by CONAE and come with the product (OFFLINE_FAST) and are provided after 2 days, the accuracy is listed as 70 m.

The IV processor can be supplied with a digital elevation model in any supported projection (latitude-longitude, UTM, Polar Stereographic, etc.). The DEM is projected into the SAR geometry by the interferometric processor.

The principal input for IVC are regional monthly and annually averaged maps of Antarctica, produced by the IV processing chain. For specific case studies it is possible to amend the IVC module with an option to use single-track 6 or 12 day repeat pass data.

3.4.2 Output Data

The output product of the IV processing chain is a map of the east and north of components of horizontal ice velocity provided in meters per day. The velocity grid for a single image pair represents the average ice surface velocity over the respective repeat pass period. The generation of regional ice velocity maps requires the combination of results from several tracks. These maps form the input for further derived monthly and annually averaged maps. The IVC product will be delivered as gridded maps, matching the grid size and extent of the regional IV maps it is derived from.

3.5 Accuracy and performance

OT accuracy depends on various factors, including on the level of coherence, on the correlation window size (Bamler and Eineder, 2005) as well as on the type of features that are being tracked. In addition, ionospheric scintillations can have a large impact on offset tracking by causing azimuth shifts that are introduced by the fluctuating electron density along the sensor path (see Fig. 3.4). Misregistration is not a problem, but the large azimuth shifts are interpreted as ice motion and observed offsets can exceed the azimuth pixel size. There are several options to correct for ionospheric artefacts. Over the interior parts of the ice sheets (where the velocities are stable in time) image stacking has usually been applied for the shifts in azimuth and range of the individual image pairs. The use of crossing tracks (ascending/descending) helps reduce ionospheric offsets in case of offset-tracking by putting larger weight on the LOS components of the displacement measurements. Compared to the Offset Tracking approach that yields at best an accuracy of some tens of centimetres, InSAR has the ability to estimate ground displacements with an accuracy better than a centimetre.

3.6 Capabilities and known limitations

InSAR performance for measuring ice motion is limited by a number of factors. The main limitations are:

- Ionosphere: at high latitude, the total electron content (TEC) of the ionosphere is very likely to vary (both in space and time) between two acquisitions. Different TEC introduce a phase delay related to the path travelled through the ionosphere, which can bias or mask the ice motion signal.
- Change in snow conditions: if snow surface undergoes change such as melting or snowfall, the change in the surface state can cause decorrelation. For this reason, InSAR shows better performance during the wintertime, during which snow conditions are more stable.
- Fast-moving areas: large displacements cause aliasing or decorrelation in interferograms. For this reason, fast-moving ice areas cannot be efficiently covered by Sentinel-1 C-Band data with 6-day revisit time. SAOCOM, operating at L-Band, on the other hand can also cover faster moving areas with an 8-day revisit time.

3.7 Uplift from InSAR line-of-sight velocities

The Uplift from InSAR Line-of-sight velocity product is based on intermediate products generated during the InSAR velocity processing, and thus the initial processing is essentially the same as the InSAR IV processor described above.

For each InSAR pair, generated from acquisitions typically 6 days apart, a line-of-sight velocity map is first generated by unwrapping, calibrating and geocoding the interferogram, converting the measured displacement to velocity by dividing with the temporal separation between the two acquisitions in the InSAR pair.

Once the full time series has been generated, the pixel wise median LoS-velocity is calculated and subtracted from the individual velocity maps. The purpose of this is to remove the bulk of the horizontal ice flow velocity contribution to the LoS velocity, making observation of small-scale uplift/subsidence phenomena easier. This means, however, that variations in the horizontal flow velocity (which can be correlated with the transients) will still be visible in the data, although they tend to be much more spatially correlated than the uplift/subsidence phenomena. Following this, the LoS velocity anomaly is converted to a displacement by multiplying with the temporal separation for each interferogram. Finally, under the assumption that the residual signal is purely due to vertical displacement, Line-of-sight displacement anomaly is converted to vertical displacement, The geocoded LoS velocity maps from several acquisitions on the same track are then stacked to form a timeseries, and the pixelwise median of the timeseries is subtracted, such that the output product is the LoS velocity anomaly, which can reveal small-scale rapid variations related to e.g. subglacial hydrological phenomena, as described in (Andersen, 2023).

3.7.1 Known Limitations

The following limitations apply to the uplift product and should be taken into account when interpreting the measurements.

1) Unwrapping errors occur when the interferometric phase unwrapping adds an incorrect number of phase cycles to the interferometric phase across a region in the image. These errors typically result in unphysical, sharply delineated regions of bias compared to the surroundings, and no measurements in such regions should be trusted.

2) Atmospheric artifacts can arise from both ionospheric scintillations, and from variations in the tropospheric water content affecting the radar signal propagation. They are typically correlated on a much larger spatial scale than the localized uplift/subsidence signals. Sometimes, the atmospheric signal arises from propagation conditions in a single image, and when this image is used in two subsequent InSAR pairs (i.e., as the first image in one interferogram and as the last image in the subsequent interferogram), the atmospheric signal reverses sign between the two resulting displacement maps.

3) All DInSAR measurements are calibrated using ground control points (GCPs) of assumed known velocity. This is done for each displacement map by fitting a plane to the observed velocity differences (measured minus known GCP velocity) and subtracting the plane fit from the displacement map. GCPs are placed across the image in slow-moving regions, i.e. outside of ice streams and glaciers, where the velocity variations are assumed negligible. Atmospheric propagation variations can, however, due to their large spatial correlation, introduce errors at many GCPs, resulting in calibration errors. These kinds of errors exhibit a bilinear variation across the image, i.e. a "tilt" of the displacement map.

4) Horizontal flow changes. Although the uplift estimate provided in this product is generated by assuming negligible horizontal flow changes, such changes do occur, especially in faster flowing regions like ice streams and glaciers.

If trying to quantify observed uplift/subsidence events, the biases introduced by the error sources described above should be accounted for, e.g. by estimating the bias in a region surrounding the uplift event.

3.8 References

Andersen, J. K., Rathmann, N., Hvidberg, C. S., Grinsted, A., Kusk, A., Merryman Boncori, J. P., & Mouginot, J. (2023). Episodic subglacial drainage cascades below the Northeast Greenland Ice Stream. Geophysical Research Letters, 50, e2023GL103240. https://doi.org/10.1029/2023GL103240

Bamler, R. and Eineder, M. (2005): Accuracy of differential shift estimation by correlation and split-bandwidth interferometry for wideband and delta-k SAR systems, IEEE Geosc. Rem Sens. Lett. 2, 151-155.

Chen, C. W. and Zebker, H. A. (2002), Phase unwrapping for large SAR interferograms: Statistical segmentation and generalized network models”,' IEEE Transactions on Geoscience and Remote Sensing, vol. 40, pp. 1709-1719.

Gray, L. (2011), Using multiple RADARSAT InSAR pairs to estimate a full three-dimensional solution for glacial ice movement. Geophysical Research Letters, 38(5).

Joughin, I., Kwok, R. and Fahnestock, M.A. (1998) Interferometric estimation of three-dimensional ice-flow using ascending and descending passes. IEEE Trans. Geosc. and Remote Sens., 36(1), 25-37.

Joughin, I. (2002). Ice-sheet velocity mapping: a combined interferometric and speckle-tracking approach. Annals of Glaciology, 34, 195-201.

Joughin, I., Smith, B. E., Howat, I. M., Scambos, T. and Moon, T. (2010). Greenland flow variability from ice-sheet-wide velocity mapping. Journal of Glaciology, 56(197), 415–430. doi:10.3189/002214310792447734

Joughin, I., Smith, B. E. and Howat, I. (2018), Greenland Ice Mapping Project: ice flow velocity variation at sub-monthly to decadal timescales, The Cryosphere, 12, 2211–2227, https://doi.org/10.5194/tc-12-2211-2018, 2018.

Mouginot, J., Rignot, E. and Scheuchl, B. (2019). Continent-wide, interferometric SAR phase, mapping of Antarctic ice velocity. Geophysical Research Letters. doi:10.1029/2019gl083826

Mouginot, J., Rignot, E., Scheuchl, B. and Millan, R. (2017), Comprehensive Annual Ice Sheet Velocity Mapping Using Landsat-8, Sentinel-1, and RADARSAT-2 Data. Remote Sens. 2017, 9, 364.

Mouginot, J., Scheuchl, B. and Rignot, E. (2012), Mapping of Ice Motion in Antarctica Using Synthetic-Aperture Radar Data. Remote Sens. 2012, 4, 2753-2767.

Nagler, T., Rott, H., Hetzenecker, M., Wuite, J. and Potin, P. (2015), The Sentinel-1 Mission: New Opportunities for Ice Sheet Observations. Remote Sens. 2015, 7, 9371-9389.

Nagler, T., Libert, L., Wuite, J., Hetzenecker, M., Keuiris, L., Rott, H.: Comprehensive Ice sheet wide velocity mapping combining SAR interferometry and offset tracking. Proc. IGARSS 2022, pp. 3888-3891, 10.1109/IGARSS46834.2022.9884206.

Rignot, E., Mouginot, J. and Scheuchl, B. (2011), Ice flow of the Antarctic Ice Sheet. Science, 333(6048), 1427–1430. https://doi.org/10.1126/science.1208336

4 Grounding Line Location and Grounding Line Migration

4.1 Introduction

The grounding line (GL) denotes all positions where the ice detaches from the bedrock and starts to float (Weertmann, 1974). The location of the GL varies due to different factors such as ocean tides, ice thickness, subglacial topography or sedimentation (Alley et al. 2007, Anandakrishnan et al. 2007). The range in which the GL naturally shifts for example due to ocean tides is called the grounding zone (GZ). The width of this zone can reach up to a few kilometres in Antarctica. A schematic cross section of the GZ is given in Figure 4.1.

Precise knowledge of the grounding line location (GLL) is important for a variety of applications – mass flux determinations in order to estimate the contribution of the cryosphere to sea level change, ice shelf monitoring, glaciological investigations of the flow behaviour and the discrimination between ocean and land as boundary condition for ice- or hydrodynamic ocean tide models.

Almost half the Antarctic coast is encased by ice shelves (Glasser and Scambos, 2008) through which 90% of the entire Antarctic ice loss takes places in form of calving or melting (Vaughan and Doake, 1996). The ice ocean interaction can trigger bottom melting and therefore causes a thinning of the ice shelf which again affects the location of the GL. A migration of the GLL can therefore be a sensitive indicator of climate change.

The short-term variation of the grounding line position has been acknowledged in recent grounding line products that annotate a grounding zone instead of single grounding lines (Rignot et al, 2023). We aim to provide the short-term temporal variations within the grounding zone but also separate this short-term position change from a long-term climatic induced position change that causes a relocation of the grounding zone. Note, that the grounding zone is different to the flexure zone which has long been observed in different tidal methods (Friedl et al, 2019). The flexure zone marks the landward and seaward extent of tide-induced ice shelf flexure and does not describe the area in which the ice shelf repeatedly rests on the ocean bed.

In order to establish realistic scenarios for climate change, it is required to understand the processes at the GZ along with the response of ice masses to changing boundary conditions (Gladstone et al., 2010; Nick et al., 2010). The IGOS Cryosphere Theme Report lists the GLL as an “important parameter for ice sheets”.

4.2 Review of scientific background

Initially a variety of ground-based measurements were used to map the GLL. Stephenson (1984) and Smith (1986 and 1991) utilized tiltmeter measurements for that purpose, while Vaughan (1994) deployed GPS measurements. Fricker et al. (2002), Anandakrishnan et al. (2007) and Masolov et al. (2006) applied radio echo sounding to detect grounding also to subglacial lakes.

In the 80s first aerial photographs and satellite images were analysed regarding slope induced grey value changes as well as marginal crevasses as indications for grounding zone location (Stephenson, 1984). Fricker et al. (2002) and Fricker and Padman (2006) furthermore used a combination of ERS and ICESat altimetry to reveal structures of the GZ.

The potential of InSAR for the mapping of the GL was demonstrated in multiple publications (Rignot et al. 1998a, 1998b, 1998c Metzig et al. 2000, Yamanokuchi et al. 2005, Goldstein et al. 1993, Rignot 2011). However, the derivation of the GL is only an indirect measurement since the upper limit of flexure (point F in Figure 4.1) can be detected using InSAR/DInSAR, but F is not identical with the GL at the bottom of the ice shelf (point G in Figure 4.1). Since F and G lay very close together the upper limit of flexure is often equated with the GL in most of the literature. We will also treat the upper limit of flexure as GL here.

Analytical solutions for a precise GLL estimation were shown from Vaughan (1995) who fit parameters of an elastic beam model into profiles perpendicular to the expected grounding line. This approach however requires knowledge/assumption on the ice density and thickness at the grounding line. Rabus and Lang (2002) provide models for different shapes and ice thicknesses but in particular if ice shelves are restrained due to their shape, varying coast lines or ice rises and rumples limitations remain.

Marsh et al. (2013) showed that differential speckle tracking of high-resolution radar images also provides indications of where the GZ is located. This approach has also been applied to Sentinel-1 data over the Larsen-C ice shelf by (Wallis et al. 2024). However, this method is much less sensitive than InSAR and cannot separate between tidally induced changes and real horizontal flow velocity changes, which might be interpreted misleadingly. A clear definition of the actual GL in the transition gradient is also complicated.

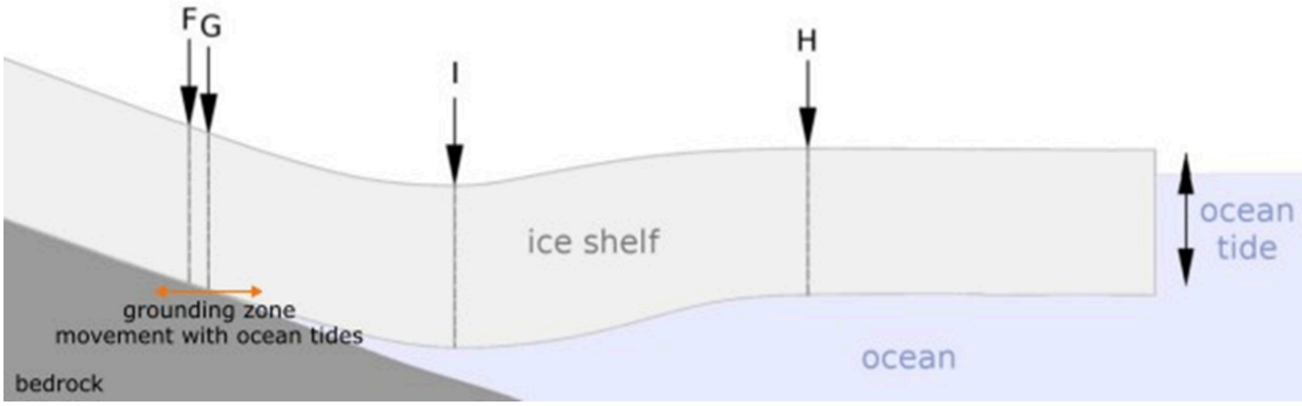

Figure 4.1: Adapted schematic cross section of the flexure zone after Vaughan (1994) and Fricker and Padman (2006). F: landward limit of flexure due to ocean tides, G: position of first floating (GL), I: reversal of gradient whereby I is located below the hydrostatic equilibrium, H: point where hydrostatic equilibrium will be reached. The fringe belt visible in differential InSAR extends from F (upper limit of flexure) to H (lower limit of flexure). The zone

4.3 Algorithm

As indicated in the previous section, several approaches were reported to measure the GLL. Among all these techniques, the InSAR double differencing method (DInSAR) has been identified to be the most accurate technique and therefore was selected in the AIS_cci project to locate the vertical tidal deformation of the ice sheet.

4.3.1 InSAR - Principle of method

For the observation of dynamic processes such as ice motion or deformation (as it occurs at the grounding zone) repeat pass interferometric synthetic aperture radar (InSAR) is a very powerful tool. The InSAR technique determines differences of phase changes of subsequent image acquisitions. These phase changes (interferogram) represent range changes in the line of sight which are usually caused by multiple factors such as baseline, topography, horizontal ice flow, deformation etc. Figure 4.2.a and b show two topography corrected interferograms of a grounding zone/line. The visible fringes are caused by horizontal ice motion as well as deformation due to height changes from ocean tides. Both effects overlap each other which make it difficult to clearly identify a GL. Figure 4.2.c in contrast depicts the interferogram difference (b-a), actually double phase differences, where the equally contained horizontal ice motion cancels and the differential vertical deformation remains. Depending on the ocean tide levels at the times of the SAR acquisitions, the resulting signal can also decrease but it will generally outline better against the background since the "disturbing" fringe pattern of horizontal ice motion is more or less completely compensated. Minor residual fringes can remain if the ice velocity is not constant over the observation period. However, this signal is too weak to hamper the appearance of the fringe belt at the GLL. As a result the GLL can be mapped in a separate process.

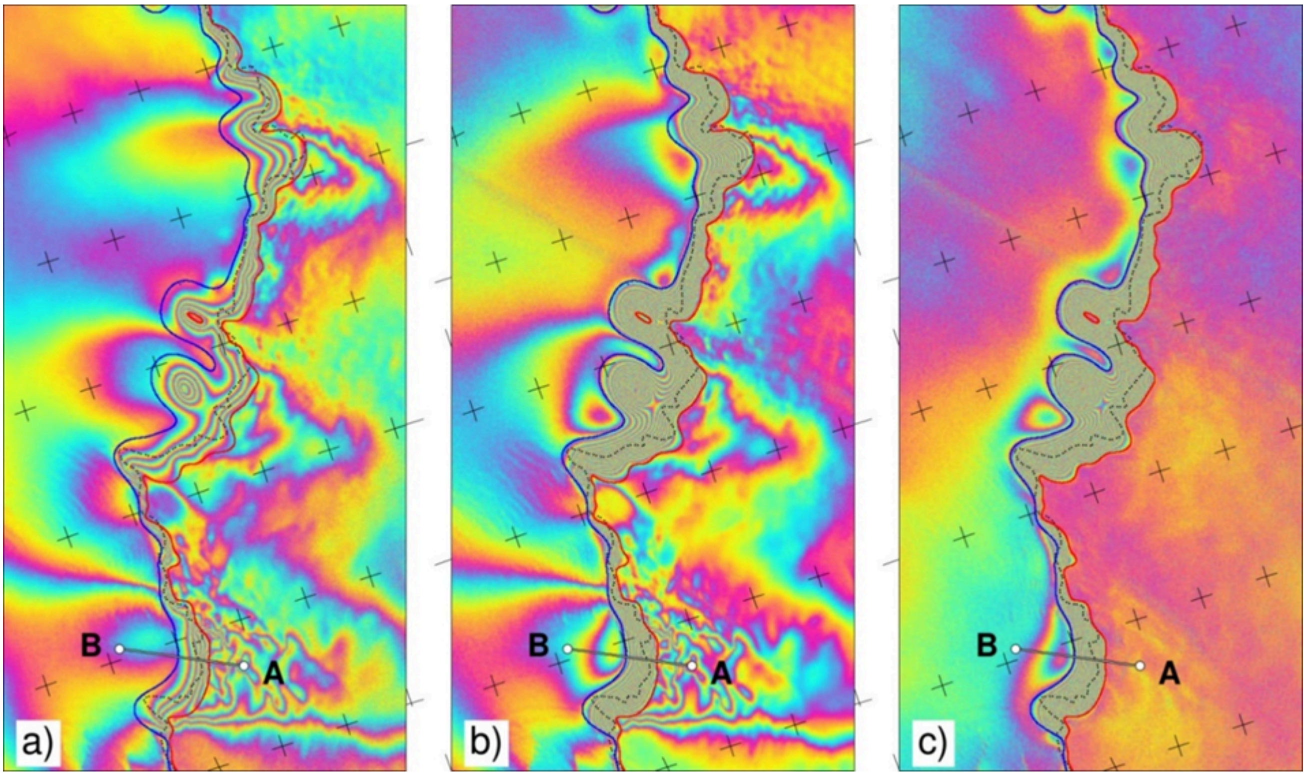

Figure 4.2 : Topography corrected interferograms of t_2-t_1 (a) and t_4-t_3 (b) which contain horizontal ice motion and deformation at the GZ due to vertical changes from ocean tides. The difference (b-a) is shown in panel c) where the effect of ice motion is cancelled. The red line represents the upper limit of flexure (point F in Figure 4.1), the blue line denotes the lower limit of flexure (point H in Figure 4.1).

4.4 Input data and algorithm output

The InSAR processing is performed with DLR's IWAP processor (Rodriguez et al. 2013, Adam et al. 2011) and starts with single look complex (SLC) data. The following paragraph shortly describes the major processing steps up to the topography corrected interferograms. Figure 4.3 shows a standard InSAR processing scheme.

If multiple image acquisitions with identical repeat orbit geometry are available (such as three or four acquisitions in a row) all scenes will be co-registered to one common master, in order to exploit the availability of all slave data sets. A cross correlation is used to estimate image-to-image shifts which is subsequently refined by a Least Squares Matching (LSM). Based on this information all slave images are resampled to the master geometry. Precise orbit information and a digital elevation model are used to determine synthetic phase images for simulations of baseline/ellipsoid and topography components. Motion only difference interferograms are obtained after the synthetic phase images were subtracted from the original interferograms. In case of multiple slave images double differences can already be determined. Depending on the interferogram coherence, a phase filtering is applied optionally. The resulting (possibly filtered) double differences are already the input data for the GL detection process.

However, in some cases there are only image pairs available which have a temporal baseline of a year or more. Each image pair has a short temporal baseline and provides a valuable interferogram but the co-registration of all scenes onto one master fails because the tracking cannot find representative points due to physical changes on ground. Since removing the motion component requires the determination of double differences, both image pairs are processed to motion only interferograms and are then geocoded. In these particular cases the GL detection will take place in the geocoded double difference interferogram, otherwise in the master image system.

At the beginning of the project the "mapping" of the grounding line was intended to manually delineate (digitize) the course of the upper flexure limit. The conducted round robin however revealed that the interpretation of the operator can be very subjective and the mapping results varied significantly depending on the shape and the quality of the interferogram. Therefore, a development towards an automatic mapping of the grounding line has to be considered.

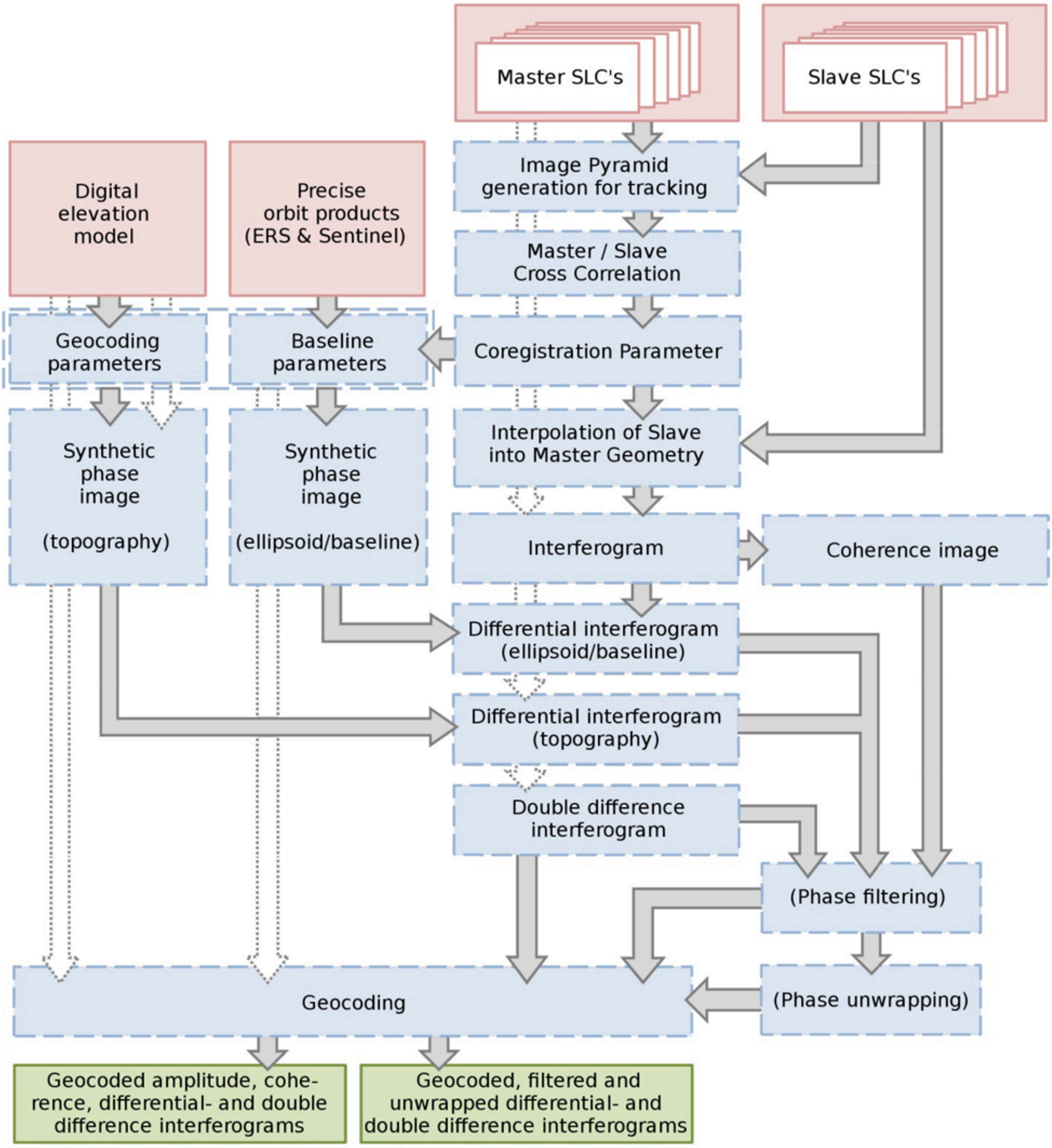

Figure 4.3 The standard InSAR processing scheme of DLR's IWAP processor (Rodriguez et al. 2013, Adam et al. 2011) adapted for grounding line double difference processing.

Since understanding the topology between grounded/floating parts, upper/lower limit of flexure, ice rises/rumple etc. can become quite difficult for complex coastlines and even more problematic for noisy interferograms where the GL is only partially exposed, the implementation of a fully automatic detection approach seems very challenging. Nevertheless, an interactive tool or a preselection would not only be very helpful to the operator but also improve the accuracy drastically since the same phase change is picked in all parts of the interferogram.

It is possible to employ machine learning approaches to automate the task of delineating grounding lines from DInSAR interferograms. By utilizing a large dataset of manually labelled ground truth labels, a neural network can be trained to accurately identify and delineate the GLs of glaciers in Antarctica. Our training data consists of manual ground truth labels, which were obtained from the Grounding Line Location produced in previous phases of ESA's Antarctic Ice Sheet climate change initiative project (AIS_cci GLL). A total of eight features is used, including eight types of interferometric and non-interferometric attributes derived from various datasets (See Figure 4.4). These features include double-difference wrapped phases, pseudo coherence (related to phase stability; has low values for high fringe frequency or decorrelated areas), surface elevation, ice velocity, tidal state, and air pressure values. A Holistically-Nested Edge Detection (HED) (Xie and Tu 2005) network is trained using this feature stack.

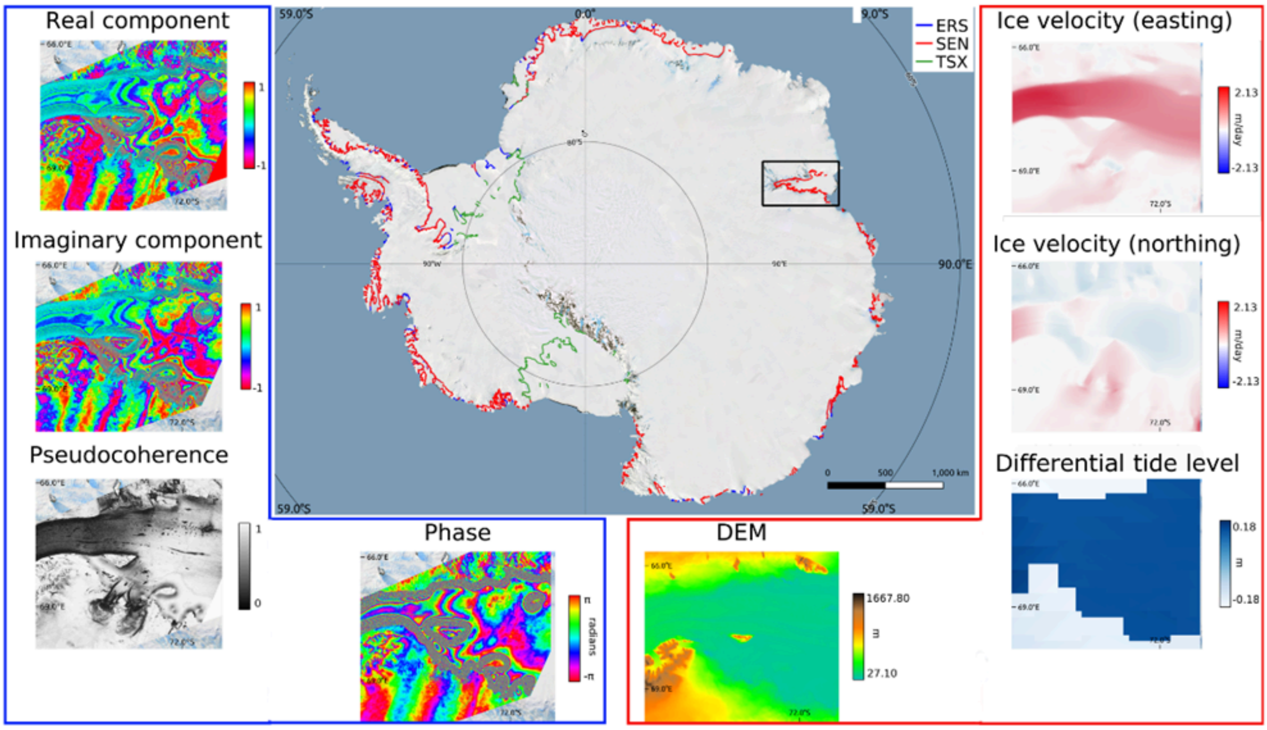

Figure 4.4 : Center map: Manual grounding line delineations from in the AIS_cci GLL dataset. The legend shows the satellite missions used to derive the DInSAR interferograms. The rectangles surrounding the map show a sample training feature stack generated for the Amery Ice Shelf (black rectangle in the center map). The red polygon encloses non-interferometric features and the blue polygon encloses interferometric features.

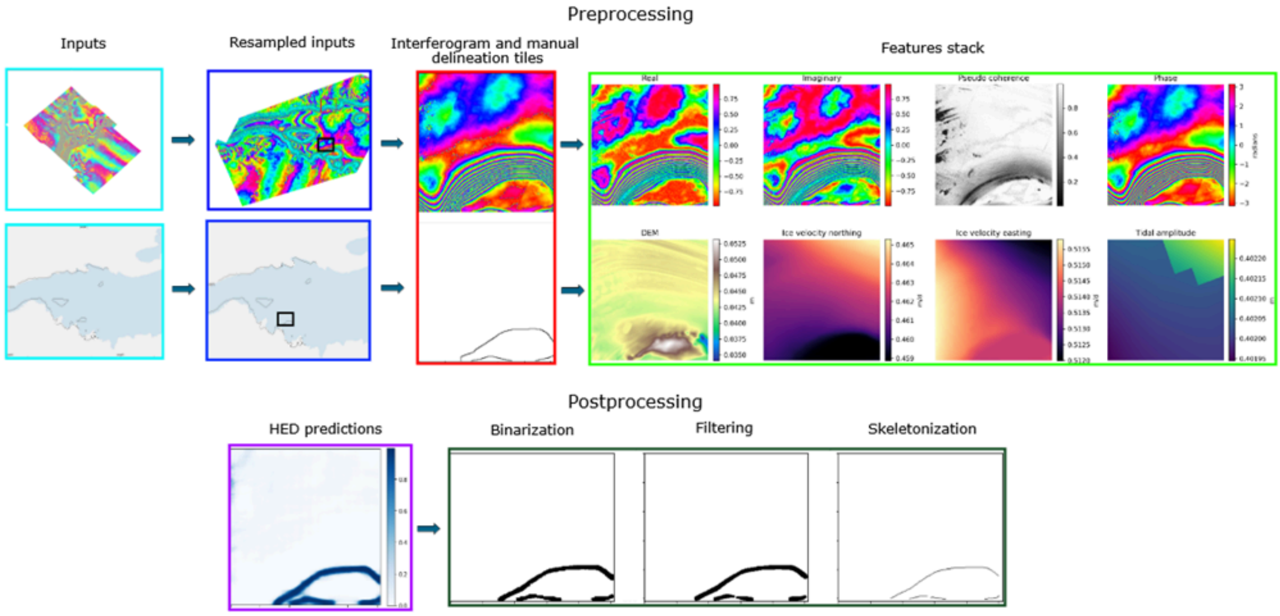

Figure 4.5 : Illustration of the steps described in the delineation pipeline flowchart (Fig. 3) for an exemplary interferogram of the Amery Ice shelf.

After training, the output segmentation maps are filtered to remove uncertain predictions using a median filter and skeletonization algorithm. We apply these filters in three stages: converting the segmentation maps to binary values, eliminating spurious branches with a median filter, and removing spurious side branches with a skeletonization algorithm.

The key steps in our approach are visualized in Figure 4.5 and include:

- Feature preparation: Converting AIS_cci GLL line geometries into rasters, resampling DInSAR interferograms, dividing features into tiles, and normalizing non-interferometric features.
- Network training: Training the HED network with weighted cross-entropy loss function and deep supervision to mitigate class imbalance and vanishing gradients.
- Segmentation map filtering: Applying a median filter and skeletonization algorithm to remove uncertain predictions.
- Output conversion: Converting line vectors to GeoJSON files.

4.5 Accuracy and performances

The accuracy of our GL geometries is evaluated using the PoLiS metric (Avbelj et al. 2014). This distance between two polygons is calculated by finding the closest point on one polygon to each vertex of another. We measure Euclidean distances between network-generated and manual GL delineations.

$$p(A,B) = \frac{1}{2|A|}\sum_{a\in A} min_{b\in B}|a-b|_2 + \frac{1}{2|B|}\sum_{b\in B} min_{a\in A}|b-a|_2$$

|A| refers to the total number of grounding line points in the ground truth and |B| is the total number of grounding line points in the network-generated GL. Additionally, we compute the coverage percentage by considering only GLs at most the median PoLiS distance away from manual GLs.

Our predictive uncertainty is estimated using an ensemble of five neural networks, with pixel-wise mean and standard deviation of predicted probabilities. The spatial uncertainty is quantified by adding one standard deviation to the mean prediction for each pixel and binarizing the values using a threshold of 0.8.

A median PoLiS distance of approximately 222 m to the ground truth labels can be expected as a result from the ensemble network. This is similar to the findings of the round robin experiment performed in a previous phase of the AIS_cci project.

4.6 Capabilities and known limitations

Differential InSAR is surely the most capable remote sensing technique for GLL detection. It works independent of sunlight and penetrates clouds which would pose problems for optical imagery. Acquisition plans allow an area wide coverage along with repeated observations of glaciers of interest. The processing chain can handle large parts of the data analysis automatically which is required for such a large area like Antarctica.

The biggest limitation on mapping the GL using DInSAR is the loss of coherence. Physical changes on ground which affect the scattering processes within one SAR resolution cell such as snow accumulation, snow drift from wind but also melting and refreezing can alter the reflected signal in a way that phase differences are no longer coherent but result in noise. Ice deformation due to strong glacier movement is also often a cause for decorrelation of the fastest glaciers in Antarctica. Consequently, the typical fringe pattern required for the indication of the GLL will not appear or is superimposed by noise.

The ERS tandem mission with a 1-day repeat cycle was optimal for that purpose. In contrast, the repeat cycles of TerraSAR-X (11 days) and Sentinel 1 (6/12 days) are significantly longer which makes such interferograms more vulnerable to decorrelation compared to interferograms of the ERS tandem mission. Phase noise itself can be filtered to some extent and is therefore not that critical. In some cases, however, particularly over quickly moving glaciers, a total loss of coherence can occur. Since the above stated reasons mainly depend on weather conditions it will be difficult to predict good or bad acquisition periods for Antarctica. An increased number of data acquisitions will compensate for this effect over time for most of the regions.

Another limitation of the DInSAR approach is the previously mentioned fact that the detected upper flexure limit is not identical with the actual grounding line itself. We are not aware of any study which compared real GLL's against DInSAR derived GLL's and quantified this effect. It is also likely that the characteristics of such a shift changes with varying ice properties, ice thickness or subglacial topography.

An important goal of the GLL mapping is the detection of grounding line retreat which involves the comparison of GLL's from different moments in time. If the GLL's are derived with the same methodology and processing strategy it can be generally assumed that this effect will further reduce in the differential case.

4.7 Round Robin conclusions

In the predecessor project AIS_cci 2015 – 2018 a Round Robin (RR) experiment has been performed. The data sets which were distributed consisted of two DInSAR interferograms: one example with ideal conditions and a second one with very difficult conditions (lots of noise and complicated shape). Participants were asked to identify and digitize the upper limit of flexure and submit the resulting vector data. The result of the RR was surprising since the GLL under perfect conditions showed an average difference of unexpected ~200 m. This 200m were due to a systematic error namely the interpretation of "where the bending starts". The random error itself was much smaller. The appearance of side fringes complicates this decision, even further decreasing the accuracy to an average difference of ~800 m to ~1.2 km in such "ambiguous" parts of the interferogram. In the very noisy interferogram provided the participants seem to zoom out onto a higher level, which provides better overview but also deteriorates the discretisation interval and consequently the accuracy. The average difference in noisy areas was ~1.5 km while single twists reached 3 km to 5 km of difference.

The major conclusion drawn from the RR experiment is that if a high accuracy and consistency of the delivered products shall be achieved and preserved over the entire project, the operator must have a tool or algorithm at hand, which either supports this decision process or better automatically segments/classifies the image. The above explained machine learning approach aims exactly in this direction and will provide reproducible GLL products.

4.8 References

Adam, N. A., Rodriguez Gonzalez, F., Parizzi, A., & Liebhart, W. (2011). Wide Area Persistent Scatterer Interferometry: Algorithms and Examples. *Proceedings of Fringe 2011, ESA SP*, ESA SP. https://earth.esa.int/eogateway/documents/20142/37627/Wide_Area_Persistent_Scatterer_Interferometry_algorithms_examples.pdf

Alley, R. B., Anandakrishnan, S., Dupont, T. K., Parizek, B. R., & Pollard, D. (2007). Effect of Sedimentation on Ice-Sheet Grounding-Line Stability. *Science*, *315*(5820), 1838–1841. https://doi.org/10.1126/science.1138396

Anandakrishnan, S., Catania, G. A., Alley, R. B., & Horgan, H. J. (2007). Discovery of Till Deposition at the Grounding Line of Whillans Ice Stream. *Science*, *315*(5820), 1835–1838. https://doi.org/10.1126/science.1138393

Avbelj, J., Müller, R., & Bamler, R. (2015). A Metric for Polygon Comparison and Building Extraction Evaluation. *IEEE Geoscience and Remote Sensing Letters*, *12*(1), 170–174. IEEE Geoscience and Remote Sensing Letters. https://doi.org/10.1109/LGRS.2014.2330695

Fricker, H. A., Allison, I., Craven, M., Hyland, G., Ruddell, A., Young, N., Coleman, R., King, M., Krebs, K., & Popov, S. (2002). Redefinition of the Amery Ice Shelf, East Antarctica, grounding zone. *Journal of Geophysical Research: Solid Earth*, *107*(B5), ECV 1-1-ECV 1-9. https://doi.org/10.1029/2001JB000383

Fricker, H. A., & Padman, L. (2006). Ice shelf grounding zone structure from ICESat laser altimetry. *Geophysical Research Letters*, *33*(15). https://doi.org/10.1029/2006GL026907

Friedl, P., Weiser, F., Fluhrer, A., & Braun, M. H. (2019). Remote sensing of glacier and ice sheet grounding lines: A review. *Earth-Science Reviews*, 102948. https://doi.org/10.1016/j.earscirev.2019.102948

Gladstone, R. M., Lee, V., Vieli, A., & Payne, A. J. (2010). Grounding line migration in an adaptive mesh ice sheet model. *Journal of Geophysical Research: Earth Surface*, *115*(F4). https://doi.org/10.1029/2009JF001615

Glasser, N. F., & Scambos, T. A. (2008). A structural glaciological analysis of the 2002 Larsen B ice-shelf collapse. *Journal of Glaciology*, *54*(184), 3–16. https://doi.org/10.3189/002214308784409017

Goldstein, R. M., Engelhardt, H., Kamb, B., & Frolich, R. M. (1993). Satellite Radar Interferometry for Monitoring Ice Sheet Motion: Application to an Antarctic Ice Stream. *Science*, *262*(5139), 1525–1530. https://doi.org/10.1126/science.262.5139.1525

Gonzalez, F. R., Adam, N., Parizzi, A., & Brcic, R. (2013). *The Integrated Wide Area Processor (IWAP): A Processor For Wide Area Persistent Scatterer Interferometry*. *722*, 353. ESA Living Planet Symposium.

IGOS, Integrated Global Observing Strategy Cryosphere Theme Report - For the Monitoring of our Environment from Space and from Earth, Geneva: World Meteorological Organization, WMO/TD-No. 1405, 100 pp (2007).

Marsh, O. J., Rack, W., Floricioiu, D., Golledge, N. R., & Lawson, W. (2013). Tidally induced velocity variations of the Beardmore Glacier, Antarctica, and their representation in satellite measurements of ice velocity. *The Cryosphere*, *7*(5), 1375–1384. https://doi.org/10.5194/tc-7-1375-2013

Masolov, V. N., Popov, S. V., Lukin, V. V., Sheremetyev, A. N., & Popkov, A. M. (2006). Russian Geophysical Studies of Lake Vostok, Central East Antarctica. In D. K. Fütterer, D. Damaske, G. Kleinschmidt, H. Miller, & F. Tessensohn (Eds.), *Antarctica: Contributions to Global Earth Sciences* (pp. 135–140). Springer. https://doi.org/10.1007/3-540-32934-X_16

Metzig, R., Dietrich, R., Korth, W., Perlt, J., Hartmann, R., & Winzer, W. (2000). Horizontal ice velocity estimation and grounding zone detection in the surroundings of Schirmacheroase, Antarctica, using SAR interferometry. *Polarforschung*, *67*(1/2), 7–14.

Nick, F. M., Veen, C. J. V. D., Vieli, A., & Benn, D. I. (2010). A physically based calving model applied to marine outlet glaciers and implications for the glacier dynamics. *Journal of Glaciology*, *56*(199), 781–794. https://doi.org/10.3189/002214310794457344

Rabus, B. T., & Lang, O. (2002). On the representation of ice-shelf grounding zones in SAR interferograms. *Journal of Glaciology*, *48*(162), 345–356. https://doi.org/10.3189/172756502781831197

Rignot, E. (1998a). Hinge-line migration of Petermann Gletscher, north Greenland, detected using satellite-radar interferometry. *Journal of Glaciology*, *44*(148), 469–476. https://doi.org/10.3189/S0022143000001994

Rignot, E. (1998b). Radar interferometry detection of hinge-line migration on Rutford Ice Stream and Carlson Inlet, Antarctica. *Annals of Glaciology*, *27*, 25–32. https://doi.org/10.3189/1998AoG27-1-25-32

Rignot, E. (1998c). Fast Recession of a West Antarctic Glacier. *Science*, *281*(5376), 549–551. https://doi.org/10.1126/science.281.5376.549

Rignot, E. (2023). Observations of grounding zones are the missing key to understand ice melt in Antarctica. *Nature Climate Change*, 1–4. https://doi.org/10.1038/s41558-023-01819-w

Rignot, E., Mouginot, J., & Scheuchl, B. (2011). Antarctic grounding line mapping from differential satellite radar interferometry. *Geophysical Research Letters*, *38*(10). https://doi.org/10.1029/2011GL047109

Smith, A. M. (1986). Ice rumples on Ronne Ice Shelf, Antarctica. *British Antarctic Survey Bulletin*, *72*, 47–52.

Smith, A. M. (1991). The use of tiltmeters to study the dynamics of Antarctic ice-shelf grounding lines. *Journal of Glaciology*, *37*(125), 51–58. https://doi.org/10.3189/S0022143000042799

Stephenson, S. N. (1984). Glacier Flexure and the Position of Grounding Lines: Measurements By Tiltmeter on Rutford Ice Stream, Antarctica. *Annals of Glaciology*, *5*, 165–169. https://doi.org/10.3189/1984AoG5-1-165-169

Vaughan, D. G. (1994). Investigating tidal flexure on an ice shelf using kinematic GPS. *Annals of Glaciology*, *20*, 372–376. https://doi.org/10.3189/1994AoG20-1-372-376

Vaughan, D. G. (1995). Tidal flexure at ice shelf margins. *Journal of Geophysical Research: Solid Earth*, *100*(B4), 6213–6224. https://doi.org/10.1029/94JB02467

Vaughan, D. G., & Doake, C. S. M. (1996). Recent atmospheric warming and retreat of ice shelves on the Antarctic Peninsula. *Nature*, *379*(6563), 328–331. https://doi.org/10.1038/379328a0

Wallis, B. J., Hogg, A. E., Zhu, Y., & Hooper, A. (2024). Change in grounding line location on the Antarctic Peninsula measured using a tidal motion offset correlation method. *The Cryosphere*, *18*(10), 4723–4742. https://doi.org/10.5194/tc-18-4723-2024

Weertman, J. (1974). Stability of the Junction of an Ice Sheet and an Ice Shelf. *Journal of Glaciology*, *13*(67), 3–11. https://doi.org/10.3189/S0022143000023327

Xie, S., & Tu, Z. (2015). *Holistically-Nested Edge Detection*. 1395–1403. https://openaccess.thecvf.com/content_iccv_2015/html/Xie_Holistically-Nested_Edge_Detection_ICCV_2015_paper.html

Yamanokuchi T., Doi K., & Shibuya K. (2005). Validation of grounding line of the East Antarctic Ice Sheet derived by ERS-1/2 interferometric SAR data. *Polar geoscience*, *18*, 1–14.

5 Gravimetric Mass Balance

5.1 Introduction

The GRACE (2002-2017, Tapley et al., 2019) and GRACE-FO (launched 2018, Landerer et al., 2020) satellite gravity missions (both referred to as GRACE in the following) allow to observe temporal changes of Earth's gravitational field. The temporal gravity variations are caused by mass redistributions within the solid Earth (mainly glacial-isostatic adjustment (GIA) and tectonics) and at the Earth's surface (water, ice, atmosphere). If the gravity effects of solid-Earth processes are known and subtracted, the remaining temporal gravity field variations can be converted into temporal variations of the surface mass distribution (in units of mass per surface area). Integration over predefined regions (such as the AIS or one of its drainage basins) leads to estimates of temporal variations of surface mass in this region. Hence, satellite gravimetry is unique in its direct sensitivity to mass changes.

The following chapter provides the theoretical basis of the algorithms used for the production of gravimetric mass change products. More details are provided in the paper by Groh and Horwath (2021) and Döhne et al. (2023)

5.2 Review of scientific background

GRACE-derived Level-2 solutions of the Earth's time variable gravity field are provided by the official processing centres of the GRACE Science Data System (SDS) at CSR, GFZ and JPL as well as by additional processing facilities like TU Graz. The COST-G service of the International Association of Geodesy also provides combined solutions, such as the latest COST-G RL02 solutions (Meyer et al., 2024). Level-2 products, provided as spherical harmonic coefficients (Stokes coefficients), are widely used in mass change studies. Alternative approaches to mass change estimates, so-called Level-1-based mascon solutions, are directly based on Level-1B data (Loomis et al. 2019a, Wiese et al. 2016). Because of differing processing strategies and background models, the comparison of various GRACE solutions reveals non-negligible differences.

With a typical temporal resolution of one month, GRACE Level-2 products allow the investigation of seasonal and inter-annual variations in addition to long-term changes (Horwath *et al.*, 2012a). Since small-scale gravity changes are attenuated at satellite altitude, the measurements are unable to resolve mass changes of high spatial resolution. The limited spatial resolution complicates the separation of mass changes from adjacent regions (e.g. neighbouring drainage basins or between ice sheet and ocean) and is the main reason for an error source termed leakage error.

Monthly GRACE solutions are affected by correlated errors. Manifesting themselves in terms of north-south oriented stripes in the spatial domain, they have to be taken into account during the inference of mass change. Various filter approaches have been proposed for minimizing GRACE error effects. These approaches comprise simply Gaussian average methods (e.g. Swenson and Wahr, 2002) as well as more elaborated approaches accounting for the error characteristics (e.g. Swenson and Wahr, 2006; Kusche *et al.*, 2009). The performance of different filters, i.e. their ability to effectively remove noise (stripes) and, at the same time, retain geophysical signals, is shown in Figure 5.1 for the example of a single monthly GRACE solution.

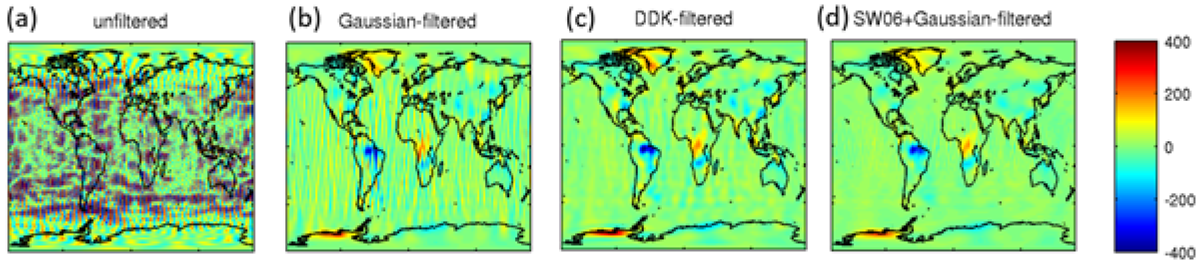

Figure 5.1: Monthly GRACE solution as of January 2008 from the series ITSG-Grace2016 by TU Graz expanded up to degree 90 (a). Different filters have been applied: Gaussian smoothing with 300km half width (b), DDK3 filter (Kusche et al., 2009) (c) and decorrelation filter of Swenson and Wahr (2006) in combination with a 300km Gaussian smoothing (d). Units: mm w.e.

While correlated errors are predominantly affecting the short wavelength (i.e. coefficients of higher spherical harmonic degrees), coefficients of low degrees are also subject to errors. In particular, C_{20} can only be imprecisely resolved from GRACE observations. To overcome this limitation C_{20} is often replaced by an estimate derived from Satellite Laser Ranging (Loomis et al., 2019b). More fundamentally, GRACE is completely insensitive to mass redistribution patterns of SH degree 1 because the observable gravity field refesr to the Earth's centre of mass (CM), where the combined degree-one effect of surface mass changes and deformations of the solid Earth is zero by definition. To avoid the omission of degree-1 information on surface mass changes, degree-1 coefficients are calculated by combining the monthly solutions and assumptions on ocean mass redistribution (Swenson et al., 2008, Sun et al., 2016).

The integrative character of GRACE observations does not allow the vertical separation between super-imposed mass changes. External information is needed to distinguish between ice mass changes and solid Earth mass redistributions caused by GIA. Deficiencies in GIA models add another potential source of errors.

5.3 Algorithm

5.3.1 Tailored sensitivity kernels: finding the compromise between GRACE noise and leakage

Methods used for the inference of mass changes from GRACE data have followed two groups of approaches: regional integration approaches (or direct approaches) and mascon approaches (or inverse approaches, or forward modeling approaches).

Based on the Round Robin experiment in the first phase of the AIS_cci project, published by Groh et al. (2019), one version of the regional integration approach has been adopted for the GMB product generation. Therefore, the focus of the following discussion is on regional integration approaches in general. However, mascon approaches and regional integration approaches are not as distinct from each other as it might appear. It has been shown (Horwath and Dietrich, 2009, Jacob *et al.*, 2012) that mascon approaches that are based on Level-2 solutions can be expressed in terms of regional integration approaches. Döhne et al. (2023) elaborated the equivalence of regional integration approaches and mascon approaches under the condition that both are formally optimized using the same stochastic characterization of GRACE solution errors and of the actual geophysical mass redistribution signal. Such a formal optimization is applied for the regional integration approach implemented for the AIS_cci+ GMB product (Groh and Horwath 2021): the tailored sensitivity kernel method. Hence, the two approaches can be considered as two complementary perspectives on the same method.

In the regional integration approach (Swenson and Wahr, 2002; Horwath and Dietrich, 2009) the mass change for a certain region *k* is estimated as:

$$\Delta m^{\wedge k} = R^2 \iint \vartheta^k(\lambda, \varphi) \Delta\kappa(\lambda, \varphi) dA$$

Here, (λ, φ) are spherical longitude and latitude, $\Delta\kappa$ is the surface mass density change [kg/m², or mm w.e.] derived from the GRACE solutions, $\vartheta^k(\lambda, \varphi)$ is the averaging kernel (1 inside, 0 outside the region), also referred to as sensitivity kernel, and the integration is over the entire sphere. To account for the limited spectral resolution of the GRACE monthly solutions and for their representation in the spherical harmonic domain, $\vartheta^k(\lambda, \varphi)$ can be expressed in the spherical harmonic domain:

$$\vartheta^k(\lambda, \varphi) = \sum_{n=0}^{n_{max}} \sum_{m=-n}^{n} \vartheta^k_{nm} Y_{nm}(\lambda, \varphi)$$

where ϑ^k_{nm} are the spherical harmonic coefficients of ϑ^k and $Y_{nm}(\lambda, \varphi)$ are the spherical harmonic base functions of degree *n* and order *m*. Together with $\Delta\kappa(\lambda, \varphi)$ expressed analogously in the spherical harmonic domain,

$$\Delta\kappa(\lambda, \varphi) = \sum_{n=0}^{n_{max}} \sum_{m=-n}^{n} \Delta\kappa_{nm} Y_{nm}(\lambda, \varphi)$$

the mass change estimate can be expressed in the spherical harmonic domain as

$$\Delta m^{\wedge} = 4\pi R^2 \sum_{n=0}^{n_{max}} \sum_{m=-n}^{n} \eta^k_{nm} \Delta\kappa_{nm}.$$

Before GRACE monthly solutions $\Delta\kappa_{nm}$ can be used within a regional integration approach inherent error effects need to be reduced by means of an appropriate filter. Usually the filtering causes an additional smoothing and attenuation of the signal leading to increased leakage. Several leakage corrections have been proposed. For examples, the derived mass change can be rescaled using a scaling factor derived by means of a synthetic high-resolution data set, e.g. a geophysical model simulating the mass change under investigation. After limiting the synthetic data set to the spatial resolution of the GRACE data and applying the filter, the scaling factor can be derived by comparing the original and the processed synthetic data (Landerer and Swenson, 2012).

Instead of performing these processing steps individually a tailored sensitivity kernel $\eta(\lambda, \varphi)$ can be designed, providing a trade-off between the minimisation of both GRACE error effects and leakage errors. From a set of regions, e.g. Antarctic drainage basins, denoted by indices k = 1,…, K, a coherent set of sensitivity kernels $\eta^k(\lambda, \varphi)$ (k = 1,…,K) is constructed. The sensitivity kernel for any region needs to be chosen as a compromise between the following conflicting conditions:

(A) Mass changes inside the region are correctly recovered

(B) Mass changes outside the region have zero influence on the regional mass change estimate

(C) Propagated errors of the GRACE solutions have small influence on the estimate.

Conditions (A) and (B) are to minimize leakage effects, while condition (C) is to minimize GRACE error effects. Tailoring of the sensitivity functions is accomplished in a formal least square adjustment procedure. The parameters to be adjusted are the spherical harmonic coefficients of the sensitivity functions, η^k_{nm}. To control leakage, condition equations on the set of coefficients η^k_{nm} need to be established for a large number of mass change patterns, where different weights can be controlled by scaling the mass patterns. For the case of Antarctica three groups of conditions can be established.

(A1) Conditions for the AIS area. They are based on point masses on a dense grid. For each of these points and for each of the regions *k,* a condition equation of the type (A) or (B) is established depending on whether the point lies inside or outside the region *k.*

(B1) Conditions outside the Antarctic ice sheet. They are based on point masses on a somewhat coarser, yet globally extended grid. For each of those points and each region *k*, conditions of type (B) were established. Points near the ice sheet may be given smaller weights to reduce the attenuation of ice mass signals close to the shoreline.

(C1) Since it is important that ice mass changes at the ice sheet margin are correctly recovered, the limited spatial resolution entails that oceanic mass changes near the ice sheet margin are inevitably sampled with a weight larger than zero. Unfortunately, due to variations of the Antarctic Circumpolar Current not completely captured by the GRACE oceanic background model, coherent oceanic mass fluctuations exist around Antarctica, which may sum up to a considerable disturbing signal for ice mass balance estimates. We therefore establish additional conditions for the adjacent ocean, which state that the sensitivity function is zero not point-wise but in an integral over a coastal zone surrounding the continent.

To establish a condition for (C) (control on propagated GRACE error effects), an error variance-covariance model for the GRACE monthly solutions, expressed as a variance-covariance matrix *C*, is needed. An error variance-covariance model may be derived empirically, e.g. based on the short-term month-to-month scatter of the monthly solutions or it may be based on the formal error covariance matrix (if available) that comes together with the GRACE monthly solutions.

In addition to basin average products, mass change grids are produced, mainly as a tool for visualisation. For this purpose, a sensitivity kernel needs to be designed for each individual grid cell. Practically, the sensitivity kernel for a basin is the sum of sensitivity kernels of the grid cells that belong to that basin.

One advantage of the regional integration approach is the possibility to visually inspect the spatial pattern of weights applied to the mass changes, which is the sensitivity kernel. Thus, sources of potential leakage can be assessed on global scale. Figure 5.2 illustrates sensitivity kernels through the examples of the entire AIS, Basin 22 (Pine Island Glacier), and a single 50 x 50 km² grid cell. Figure 5.3 shows the definition of drainage basins.

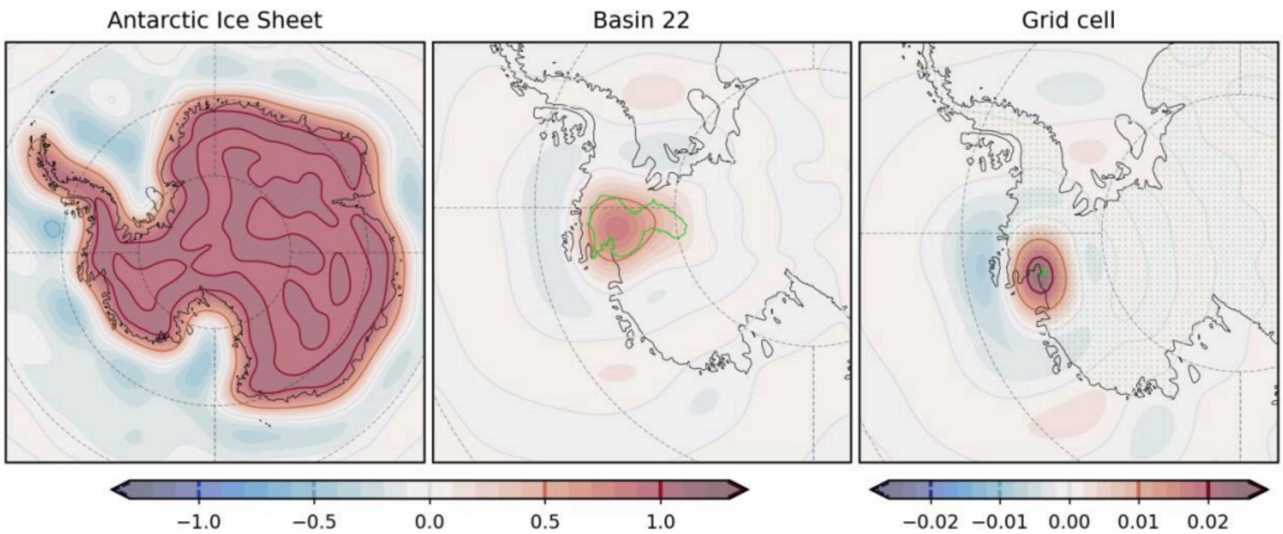

Figure 5.2: Tailored sensitivity kernels, expressed in the spatial domain, for the entire AIS (left), basin 22 (center) a single 50 x 50 km² grid cell (right).

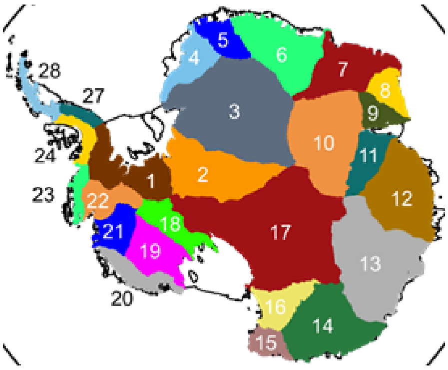

Figure 5.3: Definition of drainage basins. In addition, Basins 29, 30, 31, 32 are defined as the Antarctic Peninsula, the EAIS, the WAIS, and the entire AIS.

5.3.2 Ellipsoidal correction

The classical method to infer mass changes on the Earth surface from gravity field solutions (Wahr et al. 1998) uses the approximate assumption that mass changes occur within a thin spherical layer. More recent studies have shown that approximating the Earth ellipsoid by a sphere implies slight biases in the mass change inferences. In particular, in polar regions, the distance between the satellites and the ice sheet is actually larger than it would be under the assumption that the ice sheet is on a sphere with a radius equal to the Earth ellipsoid's semi-major axis. After reviewing methods to account for the ellipsoidal model of the Earth surface (Chao 2016; Ditmar et al. 2018; Ghobadi-Far et al. 2019) we have selected and implemented the ellipsoidal correction by Ditmar et al. (2018) which renders the Earth-radius latitude-dependent within a formally spherical-harmonic framework. Figure 5.4 illustrates the effect of the ellipsoidal correction for the mass change time series of entire AIS.

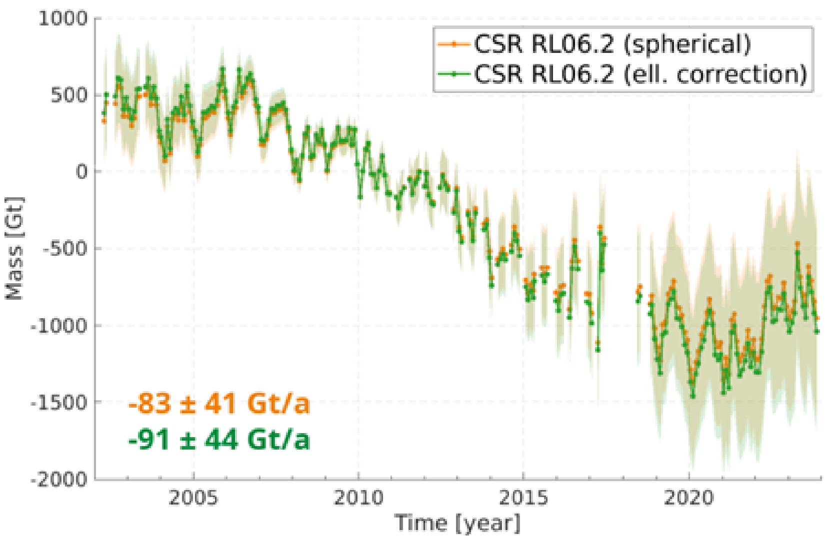

Figure 5.4: Effect of introducing the ellipsoidal correction. AIS mass anomalies without (orange) and with (green) ellipsoidal correction.

5.3.3 GRACE – GRACE-FO gap filling

There is a one-year gap between the availability of GRACE solutions (until 2017-06) and GRACE-FO solutions (from 2018-06). Methods to fill the gap between GRACE and GRACE-FO proposed in the literature include methods based on complementary gravity field observation, data-driven interpolation, and interpolation using modelled mass redistribution (Prevost et al. 2019, Yi and Sneeuw 2021, Zhang et al. 2021, Lecomte et al. 2024). Most of the studies address global analyses. For the AIS_cci+ GMB product we take advantage of the focus on the AIS, which allows to introduce established modeling results on short-term to interannual mass variations through SMB fluctuations. The very good agreement of SMB modeling results with GRACE on non-secular time scales has been demonstrated previously (Velicogna et al. 2020, Willen et al. 2020, Groh and Horwath 2021). Our method is hence based on the assumption that ice mass change is the combination of long-term changes that are relatively smooth in time and intra-annual to inter-annual changes that are well described by the cumulative SMB anomalies (cSMBA) predicted by regional atmospheric climate models such as RACMO2.3 and RACMO2.4 (van Wessem et al. 2018, van Dalum et al. 2024).

The general algorithm of gap-filling is hence the following:
(1) Reduce the cSMBA effect from the GRACE GMB time series. The result is mainly long-term change due to ice-flow dynamics, errors of the GIA correction, and month-to-month noise due to the errors of the GRACE gravity field solutions.
(2) Interpolate the data gap through fitting an analytical function within a restricted time interval around the gap.
(3) Re-add the modelled cSMBA.

Prior to ingesting cSMBA effects into this procedure, they have to be converted to the spatial resolution of the GRACE GMB. For this purpose, cSMBA is amended by its passive mass-conserving sea-level fingerprint, converted to the gravity field effect and subsequently processed in the same way as GRACE monthly solutions are processed to derive gridded and basin-average mass changes.

5.4 Input data and algorithm output

Monthly GRACE solutions of the series CSR RL06.2 by the Center for Space Research at the University of Texas at Austin expanded up to degree 90 were chosen as the basis of mass balance estimates. Using the series expanded up to degree 90 (instead of additionally available solutions expanded to degree 60) is essential for pushing the spatial resolution for the inference of regionally integrated mass changes as well as gridded products. An error variance-covariance model is empirically derived from this series, as described by Groh and Horwath (2021).

We add degree-1 coefficients derived by combining the monthly solutions and assumptions on ocean mass redistribution (Swenson et al., 2008, Sun et al., 2016). These degree-1 series are similar to those provided in TN-13 by the GRACE/GRACE-FO Science Data System (SDS), but are derived in-house consistent with the utilized GIA correction. We replaced C20 coefficients with estimates based on satellite laser ranging provided in TN-14 (Loomis et al., 2019b). We replaced C30 coefficients by TN-14 values for the time period starting from October 2016 in response to the GRACE and GRACE-FO accelerometer instrument issues (Loomis et al., 2019b).

Additional external data sets, such as geophysical models, are required for a comprehensive error assessment. Especially leakage errors can only be quantified using synthetic data set with an a priori known mass change. Data to be utilised in this context are described in the End-to-End ECV Uncertainty Budget (E3UB).

Linear trends in mass change due to GIA are corrected using a GIA model. Since global GIA models like ICE-6G_D (Peltier et al. 2018) tend to overestimate GIA in Antarctica, regional reconstructions like IJ05_R2 (Ivins *et al.*, 2013) or W12a

(Whitehouse *et al.*, 2012) are preferable. Here, we make use of the predictions according to the IJ05_R2 model based on an Earth model with a lithospheric thickness of 65 km, an upper mantle viscosity of $0.2*10^{21}$ Pa*s and a lower mantle viscosity of $1.5*10^{21}$ Pa*s (Ivins et al., 2013).

Using these input data mass change time series per basin and gridded mass change products are generated with a formal spatial resolution of 50km, given in a polar-stereographic projection. For an overview on the considered drainage basins see Figure 5.3

5.5 Accuracy and performances

The accuracy of the derived mass changes is mainly limited by the three dominating error effects: (a) errors of the GRACE solutions, (b) leakage errors, and (c) errors in correcting superimposed non-ice-mass signals such as GIA. A suitable processing is required to limit the propagation of GRACE errors to derived mass changes. Leakage errors are caused by the limited spatial resolution and possibly reinforced by the applied processing (filtering). Thus, the error of the mass change estimates strongly depends on the algorithm's ability to minimize the sum of GRACE errors and leakage errors. The regional integration approach using tailored sensitivity kernels allows to control this trade-off by means of weights put on the different conditions. Errors of the GIA correction depend on the fidelity of the GIA model applied and can be reduced only by improving GIA modeling (Whithouse 2018) or the inference of GIA from geodetic data combination techniques (Willen et al. 2024).

For assessing the performance of the algorithm external data sets are required. Mass change products can be compared with those derived by alternative methods (input-output method or geometric method). Since these methods are not able to directly observe mass changes additional information, e.g. a firn compaction model for the volume-to-mass conversion of SEC products, are required. Because the observations and the model corrections are also afflicted by uncertainties, the comparison with GRACE-derived mass change products is difficult and of limited reliability.

The most suitable strategy for assessing the performance of the algorithms is by means of synthetic data sets with an a priori known true signal of high resolution. Such tests have been performed within the open Round Robin experiment (Groh et al. 2019).

5.6 Capabilities and known limitations

The strength of the gravimetric method lies in the integrative character of GRACE observations. The integral effect of mass redistributions is observed, and therefore there are no lacks of sampling which are typical for the two complementary methods (Input-output method and geometric method). Moreover, the monthly sampling allows to detect temporal variations in surface mass beyond long-term changes.

The main limitation consists of the limited spatial resolution which prohibits the determination of small scale mass changes at the scale of individual glaciers and induces leakage errors. However, the regional integration approach allows to assess the expected leakage by visualising the sensitivity kernel.

Since most of the presently glaciated regions are experiencing GIA, the determination of ice mass changes from GRACE data inevitably depends on the utilisation of complementary information, typically a GIA model. Uncertainties in the model predictions are directly propagated to the mass change estimates.

5.7 References

Chao BF (2016) Caveats on the equivalent water thickness and surface mascon solutions derived from the GRACE satellite-observed time-variable gravity. J Geod 90(9):807{813. https://doi.org/10.1007/s00190-016-0912-y

Ditmar P (2018) Conversion of time-varying Stokes coefficients into mass anomalies at the Earth's surface considering the Earth's oblateness. J Geod. 92(12):1401{1412. https://doi.org/10.1007/s00190-018-1128-0

Döhne, T., Horwath, M., Groh, A., & Buchta, E. (2023). The sensitivity kernel perspective on GRACE mass change estimates. Journal of Geodesy, 97(1), 11, https://doi.org/10.1007/s00190-022-01697-8

Ghobadi-Far, K., Sprlak, M., and Han, S.-C. (2019). Determination of ellipsoidal surface mass change from grace time-variable gravity data. Geophysical Journal International, 219(1):248–259

Groh, A., Horwath, M., Horvath, A., Meister, R., Sørensen, L. S., Barletta, V. R., Forsberg, R., Wouters, B., Ditmar, P., Ran, J., Klees, R., Su, X., Shang, K., Guo, J., Shum, C. K., Schrama, E., Shepherd, A.2 (2019). Evaluating GRACE Mass Change Time Series for the Antarctic and Greenland Ice Sheet—Methods and Results. Geosciences, 9(10), 415. DOI: 10.3390/geosciences9100415

Groh, A., M. Horwath (2021): Antarctic Ice Mass Change Products from GRACE/GRACE-FO Using Tailored Sensitivity Kernels. Remote Sensing, 13, 1736, https://doi.org/10.3390/rs13091736

Horwath, M., and Dietrich, R. (2009). Signal and error in mass change inferences from GRACE: the case of Antarctica. Geophys. J. Int., 177(3), 849–864.

Jacob, T., Wahr, J., Pfeffer, W. T., and Swenson, S. (2012). Recent contributions of glaciers and ice caps to sea level rise. Nature, 482, 514–518.

Kusche, J., Schmidt, R., Petrovic, S., and Rietbroek, R. (2009). Decorrelated GRACE time-variable gravity solutions by GFZ, and their validation using a hydrological model. J. Geod., 83(10), 903–913.

Landerer, F. W., and Swenson, S. C. (2012). Accuracy of scaled GRACE terrestrial water storage estimates. Water Resources Research, 48(4).

Lecomte, H., Rosat, S., & Mandea, M. (2024). Gap filling between GRACE and GRACE-FO missions: assessment of interpolation techniques. Journal of Geodesy, 98(12), 1-19. https://doi.org/10.1007/s00190-024-01917-3

Loomis BD, Luthcke SB, Sabaka TJ (2019a) Regularization and error characterization of GRACE mascons. J Geod 93:1381–1398. doi: 10.1007/s00190-019-01252-y

Loomis BD, Rachlin KE, Luthcke SB (2019b) Improved earth oblateness rate reveals increased ice sheet losses and mass-driven sea level rise. Geophys Res Lett 46:6910–6917. https://doi.org/10.1029/ 2019GL082929

Peltier, W. R., Argus, D. F., and Drummond, R.: Comment on "An Assessment of the ICE-6G_C (VM5a) Glacial Isostatic Adjustment Model" by Purcell et al., J. Geophys. Res. Solid Earth, 123, 2019–2028, https://doi.org/10.1002/2016JB013844, 2018.

Prevost, P., Chanard, K., Fleitout, L., Calais, E., Walwer, D., van Dam, T., & Ghil, M. (2019). Data-adaptive spatio-temporal filtering of GRACE data. Geophysical Journal International, 219(3), 2034-2055. https://doi.org/10.1093/gji/ggz409

Sun, Y., Riva, R., and Ditmar, P.: Optimizing estimates of annual variations and trends in geocenter motion and J2 from a combination of GRACE data and geophysical models, J. Geophys. Res. Solid Earth, 121, 8352–8370, https://doi.org/10.1002/2016JB013073, 2016.

Swenson, S., and Wahr, J. (2002). Methods for inferring regional surface-mass anomalies from Gravity Recovery and Climate Experiment (GRACE) measurements of time-variable gravity. J. Geophys. Res., 107(B9), 2193.

Swenson, S., and Wahr, J. (2006). Post-processing removal of correlated errors in GRACE data. Geophys. Res. Lett., 33, L08402.

Swenson, S., Chambers, D., and Wahr, J.: Estimating geocenter variations from a combination of GRACE and ocean model output, J. Geophys. Res. Solid Earth, 113, https://doi.org/10.1029/2007JB005338, 2008.

van Dalum, C. T., van de Berg, W. J., Gadde, S. N., van Tiggelen, M., van der Drift, T., van Meijgaard, E., ... & van den Broeke, M. R. (2024). First results of the polar regional climate model RACMO2. 4. The Cryosphere, 18(9), 4065-4088, https://doi.org/10.5194/tc-18-4065-2024

van Wessem, J. M., van de Berg, W. J., Noël, B. P. Y., van Meijgaard, E., Amory, C., Birnbaum, G., Jakobs, C. L., Krüger, K., Lenaerts, J. T. M., Lhermitte, S., Ligtenberg, S. R. M., Medley, B., Reijmer, C. H., van Tricht, K., Trusel, L. D., van Ulft, L. H., Wouters, B., Wuite, J., and van den Broeke, M. R. (2018): Modelling the climate and surface mass balance of polar ice sheets using RACMO2 – Part 2: Antarctica (1979–2016), The Cryosphere, 12, 1479–1498, https://doi.org/10.5194/tc-12-1479-2018

Velicogna, I., Mohajerani, Y., Landerer, F., Mouginot, J., Noel, B., Rignot, E., ... & Wiese, D. (2020). Continuity of ice sheet mass loss in Greenland and Antarctica from the GRACE and GRACE Follow-On missions. Geophysical Research Letters, 47(8), e2020GL087291, https://doi.org/10.1029/2020GL087291

Wahr, J., Molenaar, M., & Bryan, F. (1998). Time variability of the Earth's gravity field: Hydrological and oceanic effects and their possible detection using GRACE. Journal of Geophysical Research: Solid Earth, 103(B12), 30205-30229, https://doi.org/10.1029/98JB02844

Whitehouse, P. L. (2018). Glacial isostatic adjustment modelling: historical perspectives, recent advances, and future directions. Earth Surface Dynamics, 6(2), 401-429, https://doi.org/10.5194/esurf-6-401-2018

Wiese DN, Landerer FW, Watkins MM (2016) Quantifying and reducing leakage errors in the JPL RL05M GRACE mascon solution. Water Resour Res 52:7490–7502. doi: 10.1002/2016WR019344

Willen, M. O., Broerse, T., Groh, A., Wouters, B., Kuipers Munneke, P., Horwath, M., & Schröder, L. (2021). Separating Long-Term and Short-Term Mass Changes of Antarctic Ice Drainage Basins: A Coupled State Space Analysis of Satellite Observations and Model Products. Journal of Geophysical Research: Earth Surface, 126(6), e2020JF005966, https://doi.org/10.1029/2020JF005966

Willen, M. O., Horwath, M., Buchta, E., Scheinert, M., Helm, V., Uebbing, B., & Kusche, J. (2024). Globally consistent estimates of high-resolution Antarctic ice mass balance and spatially-resolved glacial isostatic adjustment. The Cryosphere, 1-25, https://doi.org/10.5194/tc-18-775-2024

Yi, S., & Sneeuw, N. (2021). Filling the data gaps within GRACE missions using Singular Spectrum Analysis. Journal of Geophysical Research: Solid Earth, 126, e2020JB021227. https://doi.org/10.1029/2020JB021227

Zhang, C., Shum, C. K., Bezděk, A., Bevis, M., de Teixeira da Encarnação, J., Tapley, B. D., et al. (2021). Rapid mass loss in West Antarctica revealed by Swarm gravimetry in the absence of GRACE. Geophysical Research Letters, 48, e2021GL095141. https://doi.org/10.1029/2021GL095141

6 ISCL

6.1 Introduction

The objective of this activity is to investigate the added benefits of combining radar measurements (Sentinel-1, S1) with altimetry (CryoSat-2, CS2) in the delineation of ice shelf coastlines. This investigation is conducted over three selected ice shelves (Larsen-C, Ronne, Filchner). Those three ice shelves cover a large area and have been subject to large calving events in the recent past. Furthermore, they represent challenging areas with the simultaneous presence of glaciers and islands.

Delineation of the Ice Shelf CoastLine (ISCL) is to be performed using both SAR images from Sentinel-1 and elevation data from CryoSat-2 altimetry tracks. As a first step. the elevation data compiled from CS2 tracks provide an initial guess for the model based on elevation differences that can indicate the start of the ice shelf coastline. This initial guess, along with corresponding SAR imagery from the designated time and location from S1, is fed to a Convolutional Neural Network (CNN). The CCN combines the 2 inputs to predict a first iteration of the location of the ISCL. In the last step, the model is be run iteratively as a refinement network to refine the prediction until the location converges to the predicted ISCL.

6.2 Review of scientific background

Previous works, i.e. Baumhoer et al. 2023, used SAR imagery from S1 and a deep learning model to find the coast lines. Although this approach worked well, it has a significant drawback when it comes to sea ice. Indeed, sea ice and ice shelf ice look similar on SAR data and finding the line between them can be difficult even with the high resolution provided by SAR.

In the recent past, deep learning-based ice sheet front location delineation has been demonstrated (Icelines Baumhoer et.al.). This study evolved in a service based on Sentinel-1. However, this effort solely relies on a single data source (radar imagery), while the addition of extra data sources, such as altimetry, could disambiguate the front lines in challenging scenes where the radar data is noisy, providing a more accurate product. Single-source CryoSat-2 (CS2) swath altimetry-based front-line delineation has already been demonstrated by Wuite et al. (2019) by using traditional edge-detection techniques on gridded elevation data. The most significant limitation is temporal resolution, as several months of data acquisition are needed to generate a DEM and limited spatial resolution depending on data density. There is no solution which would combine the spatial and temporal resolution of the Sentinel-1 source and the certainty of CS2-based delineation. This activity aims at filling this gap with the development of a ML-based solution using state-of-the-art snake-adapted algorithms, a methodology never applied to this domain.

6.3 Algorithm

In this project, we explore the possibility of incorporating elevation data produced from CryoSat-2 altimeter tracks in the process. The primary added value of this elevation data is their ability to fairly distinguish sea ice from ice shelf ice along the altimeter track with high resolution (where the track is available), complementing the SAR images where the data is noisy. This is due to the clear elevation difference between the sea and the ice shelf which averages around 200 m Wuite et. al. (2019), in addition to the clarity of the altimeter data in comparison to the noisy SAR data. That provides an accurate pinpointing of where the sea (or sea ice) ends and the ice shelf begins along the acquired altimetry tracks. When that is provided, in addition to the already existing Sentinel-1 SAR imagery that provides the high resolution scene, the model can delineate the ISCLs with high certainty.

Figure 6.1 shows how SAR images can be noisy and the ISCL difficult to determine in the example of Ronnie-Filchner, with HV polarization. Figure 6.2 shows how altimetry can be more definitive in distinguishing ISCLs along the tracks where it is available, yet it lacks the temporal and spatial resolution of SAR. Figure 6.3 shows the significant elevation change in CS2 elevation data on the ISCL.

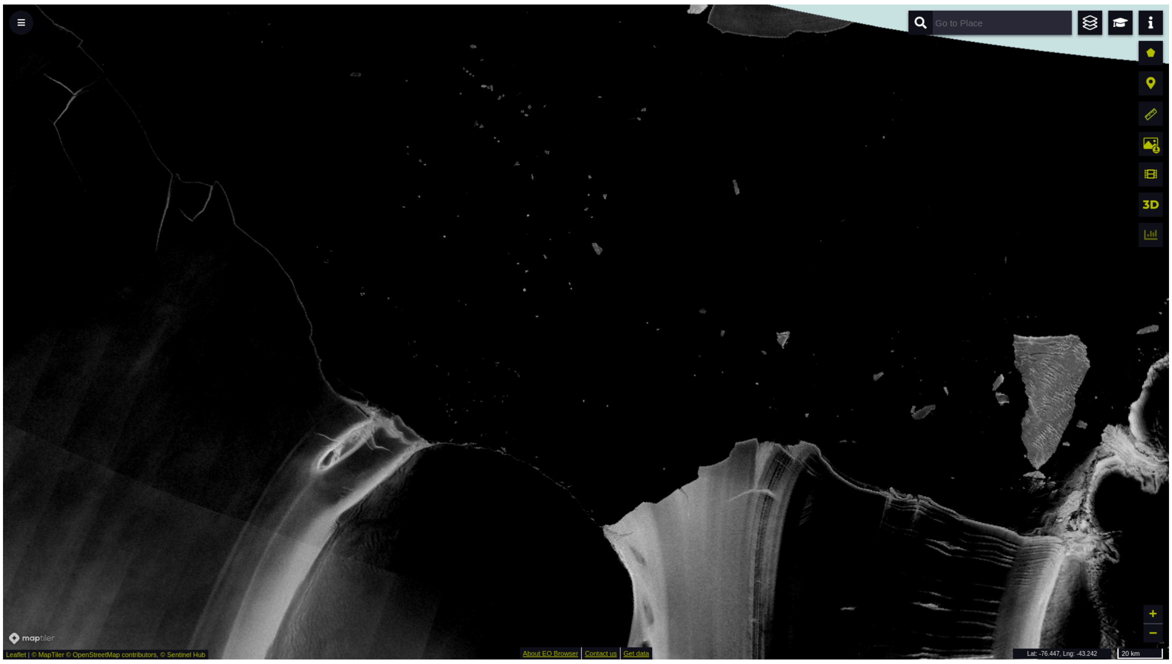

Figure 6.1: Ronnie-Filchner, HV polarization. Edges and regions are ambiguous if only S1 is available.

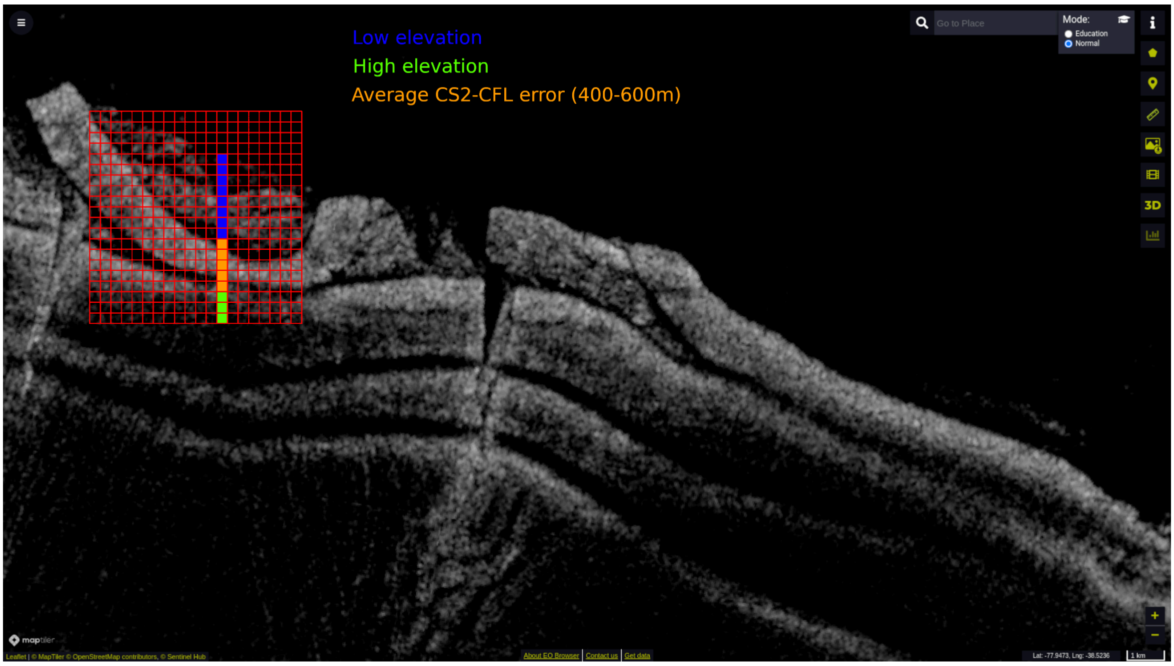

Figure 6.2: S1 can have many edges, while CS2 resolution (resampled to grid) could be locally too coarse both spatially and temporally.

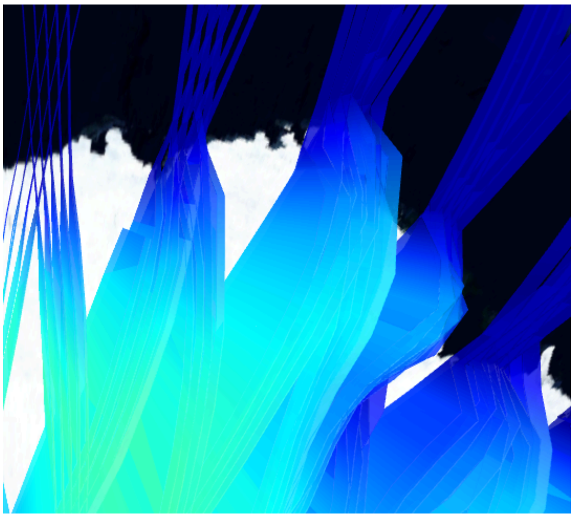

Figure 6.3: CS2 normalized elevation tracks from Retracker-1 showing the significant increase in height detected on the ice shelf.

This project is conducted over three selected ice shelves (Larsen-C, Ronne, Filchner). The selected ee ice shelves cover a large area and have been subject to large calving events in the recent past. Furthermore, they represent challenging areas with the simultaneous presence of glaciers and islands. Figure 6.4 shows these ice shelves with their yearly ISCLs from the IceLines dataset.

Figure 6.4 Ice shelves covered by the study area with their yearly ISCLs from the IceLines dataset. Images from https://geoservice.dlr.de/web/maps/eoc:icelines

Figure 6.5 shows the main workflow of the algorithm. We will describe each process in detail in the following sections.

6.3.1 Data Acquisition and Correction

First we collect the data, both SAR and Altimetry, while each one goes through a separate processing scheme.

For SAR, we use Ground Range Detected data (GRD) Sentinel-1 imagery with both Interferometric Swath mode (IW) and Extra Wide Swath mode (EW) in the mentioned areas in the time range between 2017 and 2022. We apply the typical processing workflow which includes orbit correction, border noise removal, speckle filtering, radiometric calibration, terrain flattening, and terrain correction.

For altimetry, we use CryoSat-2 Retracker-1 data for the same area and time range (it has much less spatial and temporal resolution than SAR). We then extract the dramatic elevation change points using a dynamic threshold, marking the points defining the edge of the ISCL and interpolating the acquired data to build a preliminary ISCL line. This is shown in Figure 6.3. Then the preliminary line is rasterized and prepared for further processing.

For both data types, we employ general processing where we first extract the required area of interest, re-grid the rasters to match each other and finally intersect them together spatially and temporally in preparation for inputting them to the neural network model. Furthermore, we apply data augmentation suitable for that kind of data like rotations, scaling, shifting, flipping, etc.

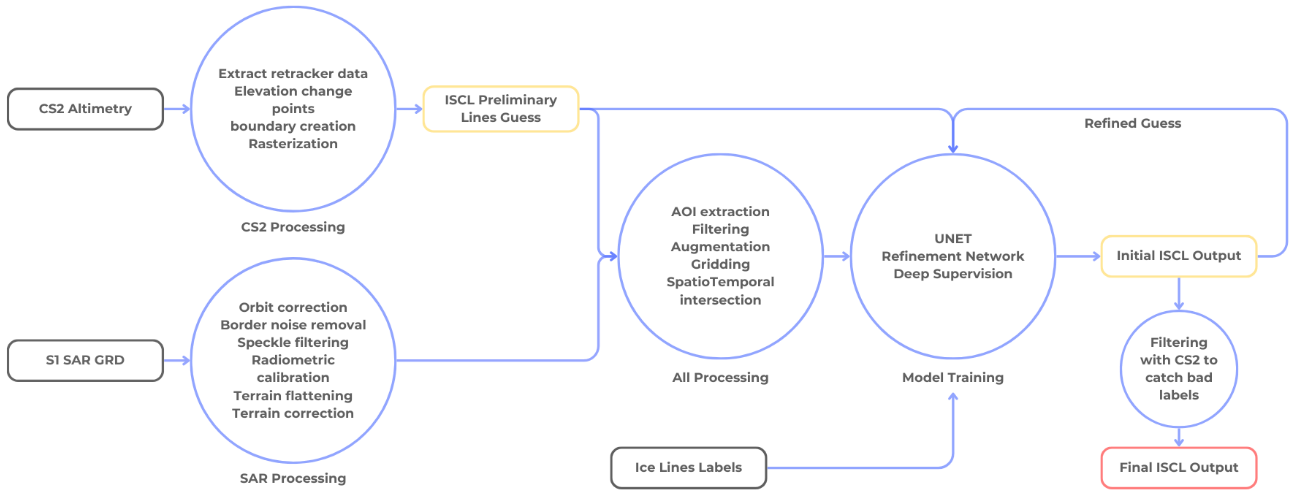

Figure 6.5: Main Workflow of the algorithm: Inputs in black borders, intermediate outputs in yellow borders, Final Output in red border. Processes in circles while data is in rectangles.

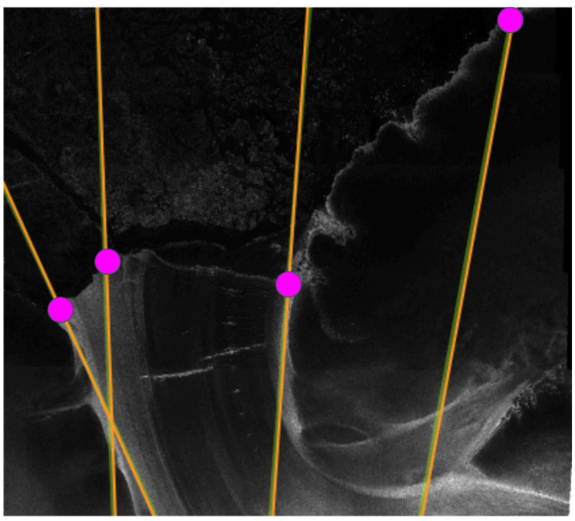

Figure 6.6: Altimetry tracks (yellow) with dramatic elevation change points marked on the edge of the ice shelf (pink).

6.3.2 Training and Refinement

The training starts using a U-net model with deep supervision where the input is a 3-channel feature map consisting of the HH and HV polarizations of the SAR scene as well as the CS2 election data. U-net models are popular in classification and segmentation tasks and can be found in all sorts of applications where they were repeatedly tested. The loss used is a tuned focal loss where each class is weighted by its relative abundance which accounts for class imbalance and gives a fair representation to all classes. The labels are used from the IceLines dataset which is generated from S1 images and at their recurrence frequency.

This network is used as a refinement network however. The initial guess coming from the CS2 data is fed to the network in addition to the feature map, and when the network outputs the initial ISCL line, it is fed back to the network as a refined guess. That loop commences in multiple iterations until saturation on inference, making an iterative refinement network that iteratively refines the output ISCL until it fits the ice shelf minimizing the error. This is shown in Figure 6.7.

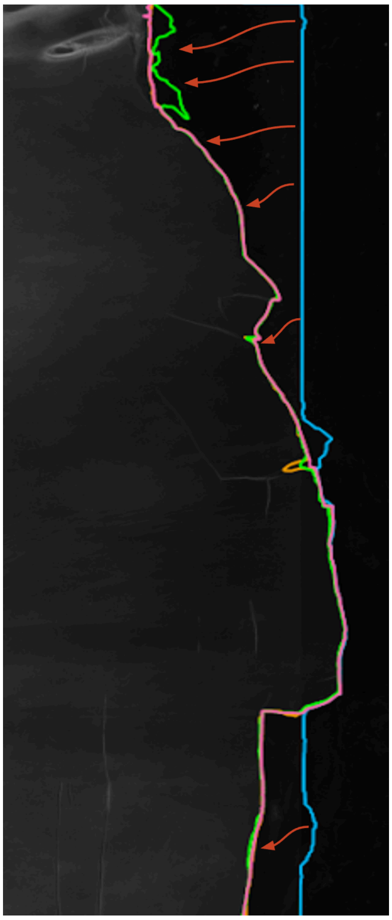

Figure 6.3.7 Iterative refinement fitting the ISCL to its correct location.

6.3.3 Filtering Bad Labels

Since the labels used are the IceLines model output, they are themselves generated from a neural network and therefore inherently flawed. That is a large limitation since using flawed data as ground truth limits the model's capability. We have no alternative but to use that data since we cannot obtain manually delineated ISCLs to use as ground truth. This problem in the labels can be seen in Figure 6.8, where the IceLines produced ISCLs have wild inconsistencies that confuse the network when used as labels. To overcome this, we use the CS2 data again to filter out samples where the CS2 elevation change does not exist or is inconsistent with the result. The difference between this filtering and the natural use of CS2 data in the network is that this is hard filtering with the knowledge that the CS2 data is highly reliable, unlike the soft learning done in the model. This overcomes many of the false positives imminent to appear in the outputs as a result of the bad labelling.

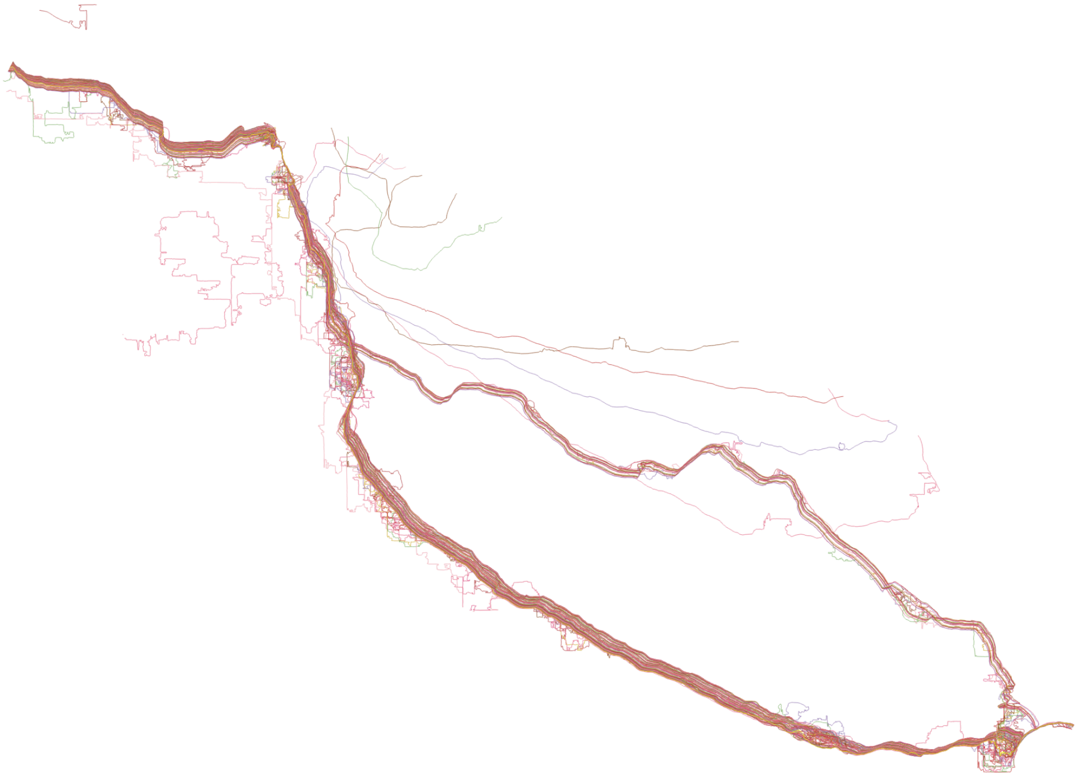

Figure 6.8: IceLines around Larsen C showing wild inconsistencies.

6.4 Input data and algorithm output

The input data consists of the following:

- SAR Ground Range Detected (GRD) from Sentinel-1 both HH and HV on IW and EW modes. Used as tif files after correction.
- Altimeter data from CS2 Retracker-1 as nc files.

The output products consist of monthly ice shelf lines for each of the ice shelves under study. The products are in the form of GeoPackage vector data (.gpkg) for easy distribution, opening, and size requirements. Each file contains multiple line strings which hold the data of the line in EPSG:3031 Antarctic Polar Stereographic CRS. The file also contains metadata containing information related to the Sentinel-1 image used to obtain the line, following the CCI data standard. This data includes acquisition time, ID, mode, polarisation, and processing type. The data extends from 2017 to 2022 across the Larsen C, Ronne(1 and 2) and Filchner ice shelves. It has a spatial resolution dependent on the S1 image mode used. Since we are using GRD images, it can reach 20 x 22 for IW and 50 x 50 for EW image modes.

6.5 Accuracy and performances

Accuracy is measured with F1 Score, a common measure capturing the performance of segmentation tasks. However, due to the labels limitation mentioned in section 6.3.3 manual validation will also be needed since achieving a high metric will only be compared to the labels which have flaws in them and might not reflect the true performance of the model.

6.6 Capabilities and known limitations

The main capability of this method is the additional CS2 elevation data that is capable of finding anchor points for the ISCL which helps in both giving an initial guess to the model and also filtering any false negatives and adjusting the result. The iterative refinement method also minimizes the error and employs the CS2 guess in the fitting.

As for limitations, the main limitation is the one already mentioned about the use of generated ISCL lines as labels which have clear flaws and limit the model's capability in learning and producing good results. The effect of that problem is minimized again using the CS2 lines as filters towards the end of the process to remove false positives.

6.7 References

Avbelj, J., Muller, R., & Bamler, R. (2014). A Metric for Polygon Comparison and Building Extraction Evaluation. IEEE Geoscience and Remote Sensing Letters, 12(1), 170–174. https://doi.org/10.1109/LGRS.2014.2330695

Baumhoer CA, Dietz AJ, Heidler K, Kuenzer C. IceLines–A new data set of Antarctic ice shelf front positions. Scientific Data. 2023 Mar 15;10(1):138.

Döhne, T., Horwath, M., Groh, A., & Buchta, E. (2023). The sensitivity kernel perspective on GRACE mass change estimates. Journal of Geodesy, 97(1), 11, https://doi.org/10.1007/s00190-022-01697-8

GCOS, 2022. The 2022 GCOS Implementation Plan. Geneva: World Meteorological Organization, 85. https://gcos.wmo.int/en/publications/gcos-implementation-plan2022

Groh, A. and Horwath, M.: Antarctic Ice Mass Change Products from GRACE/GRACE-FO Using Tailored Sensitivity Kernels, Remote Sens., 13, 1736, https://doi.org/10.3390/rs13091736, 2021.

Howat, I. M., Porter, C., Smith, B. E., Noh, M.-J., and Morin, P.: The Reference Elevation Model of Antarctica, The Cryosphere, 13, 665-674, https://doi.org/10.5194/tc-13-665-2019, 2019.

Ivins, E. R., James, T. S., Wahr, J., O. Schrama, E. J., Landerer, F. W., & Simon, K. M. (2013). Antarctic contribution to sea level rise observed by GRACE with improved GIA correction. Journal of Geophysical Research: Solid Earth, 118(6), 3126-3141, DOI: 10.1002/jgrb.50208

Landerer, F. W., Flechtner, F. M., Save, H., Webb, F. H., Bandikova, T., Bertiger, W. I., Bettadpur, S. V., Byun, S. H., Dahle, C., Dobslaw, H., Fahnestock, E., Harvey, N., Kang, Z., Kruizinga, G. L. H., Loomis, B. D., McCullough, C., Murböck, M., Nagel, P., Paik, M., Pie, N., Poole, S., Strekalov, D., Tamisiea, M. E., Wang, F., Watkins, M. M., Wen, H.-Y., Wiese, D. N., and Yuan, D.-N.: Extending the Global Mass Change Data Record: GRACE Follow-On Instrument and Science Data Performance, Geophys. Res. Lett., 47, e2020GL088306, https://doi.org/10.1029/2020GL088306, 2020.

Moon, Twila and Ian R. Joughin. „Changes in Ice Front Position on Greenland's Outlet Glaciers from 1992 to 2007". Journal of Geophysical Research: Earth Surface 113, Nr. F2 (2008). https://doi.org/10.1029/2007JF000927.

Nagler, T, Rott, H., Hetzenecker, M., Wuite, J. and Potin, P., (2015): The Sentinel-1 Mission: New Opportunities for Ice Sheet Observations. Remote Sens., 7, 9371-9389.

Shepherd, A., Gilbert, L., Muir, A. S., Konrad, H., McMillan, M., Slater, T., et al. (2019). Trends in Antarctic Ice Sheet elevation and mass. Geophysical Research Letters, 46, 8174–8183. https://doi.org/10.1029/2019GL082182

Tapley, B. D., Watkins, M. M., Flechtner, F., Reigber, C., Bettadpur, S., Rodell, M., Sasgen, I., Famiglietti, J. S., Landerer, F. W., Chambers, D. P., Reager, J. T., Gardner, A. S., Save, H., Ivins, E. R., Swenson, S. C., Boening, C., Dahle, C., Wiese, D. N., Dobslaw, H., Tamisiea, M. E., and Velicogna, I.: Contributions of GRACE to understanding climate change, Nat. Clim. Change, 9, 358–369, https://doi.org/10.1038/s41558-019-0456-2, 2019.

Wuite, J. et al. Sub-Annual Calving Front Migration, Area Change and Calving Rates from Swath Mode CryoSat-2 Altimetry, on Filchner-Ronne Ice Shelf, Antarctica. Remote Sens. 2019, 11, 2761. https://www.mdpi.com/2072-4292/11/23/2761

Zwally, H. Jay, Mario B. Giovinetto, Matthew A. Beckley, and Jack L. Saba, 2012, Antarctic and Greenland Drainage Systems, GSFC Cryospheric Sciences Laboratory, https://earth.gsfc.nasa.gov/cryo/data/polar-altimetry/antarctic-and-greenland-drainage-systems

End of document